Transition metal dissolution from Li-ion battery cathodes

YONAS TESFAMHRET

Dissertation presented at Uppsala University to be publicly examined in Polhemsalen, 10134, Ångströmlaboratoriet, Lägerhyddsvägen 1, Uppsala, Friday, 30 September 2022 at 09:15 for the degree of Doctor of Philosophy. The examination will be conducted in English. Faculty examiner: Professor Mark Huijben (University of Twente).

Abstract
Tesfamhret, Y. 2022. Transition metal dissolution from Li-ion battery cathodes. *Digital Comprehensive Summaries of Uppsala Dissertations from the Faculty of Science and Technology* 2178. 71 pp. Uppsala: Acta Universitatis Upsaliensis. ISBN 978-91-513-1572-0.

Lithium-ion batteries (LIBs) have become reliable electrochemical energy storage systems due to their relative high energy and power density, in comparison to alternative battery chemistries. The energy density of current LIBs is limited by the average operating voltage and capacity of oxide-based cathode materials containing a variety of transition metals (TM). Furthermore, the low anodic stability of "conventional" carbonate-based electrolytes limits further extension of the LIBs voltage window. Here, ageing mechanisms of cathodes are investigated, with a main focus on TM dissolution and on strategies to tailor the cathode surface and the electrolyte composition to mitigate TM dissolution.

Atomic layer deposition (ALD) coatings of the cathode surface with electrically insulating Al_2O_3 and TiO_2 coatings is employed and investigated as a method to stabilize the cathode/electrolyte interface and minimize TM dissolution. The thesis illustrates both the advantages and limitations of amorphous oxide coating materials during electrochemical cycling. The protective oxide layer restricts auto-catalytic salt degradation and the consequent propagation of acidic species in the electrolyte. However, a suboptimal coating contributes to a nonhomogeneous cathode surface ageing during electrochemical cycling. Furthermore, the widely accepted concept of charge disproportionation as the fundamental cause of TM dissolution is demonstrated to be a minor factor. Rather, a chemical dissolution mechanism based on acid-base/electrolyte-cathode interaction underlies substantial TM dissolution.

The thesis demonstrates $LiPF_6$, and by implication HF, as the principal source of TM dissolution. In addition, the oxidative degradation of ethylene carbonate (EC) solvent contributes indirectly to generation of HF. Thus, an increase in electrolyte oxidative degradation products accelerates TM dissolution. Substituting EC and $LiPF_6$ with a more anodically stable solvent (*e.g.*, tetra-methylene sulfone) and a non-fluorinated salt (*e.g.*, LiBOB or $LiClO_4$) or addition of TM scavenging additives like lithium difluorophosphate ($LiPO_2F_2$) are here investigated as strategies to either i) mitigate TM dissolution, ii) supress TM migration and deposition on the anode surface, or iii) supress formation of acidic electrolyte degradation products and thereby TM dissolution. The thesis also highlights the necessity of taking precautions when attempting to replace the components, as reducing TM dissolution may come at the expense of electrochemical cycling performance.

Keywords: Lithium-ion battery, Lithium-ion cathode, Transition metal dissolution, Atomic Layer Deposition, Inductively coupled plasma atomic emission spectroscopy, Cathode-electrolyte interaction

Yonas Tesfamhret, Department of Chemistry - Ångström, Structural Chemistry, Box 538, Uppsala University, SE-751 21 Uppsala, Sweden.

To my parents

List of Papers

This thesis is based on the following papers, which are referred to in the text by their Roman numerals.

I. **<u>Tesfamhret, Y.</u>**, Liu, H., Chai, Z., Berg, E.J., Younesi, R. (2021) On the Manganese Dissolution Process from LiMn$_2$O$_4$ Cathode Materials. *ChemElectroChem*, 8(8):15816–1523

II. Østli, E., **<u>Tesfamhret, Y.</u>**, Wenner, S., Lacey, M.J., Brandell, D., Svensson, A.M., Selbach, S.M, Wagner, N.P. (2022) Limitations of Ultrathin Al$_2$O$_3$ Coatings on LNMO Cathodes. *ACS omega*, 6(45):30644–30655

III. Østli, E., Ebadi, M., **<u>Tesfamhret, Y.</u>**, Mahmoodinia, M., Lacey, M.J., Brandell, D., Svensson, A.M., Selbach, S.M, Wagner, N.P. (2022) On the Durability of Protective Titania Coatings on High-Voltage Spinel Cathodes. *ChemSusChem*, 15(12): e202200324

IV. **<u>Tesfamhret, Y.</u>**, Younesi, R., Berg, E.J. (2022) Influence of Al$_2$O$_3$ Coatings on HF Induced Transition Metal Dissolution from Lithium-ion Cathodes. *Journal of The Electrochemical Society*, 169(1):010530

V. **<u>Tesfamhret, Y.</u>**, Liu, H., Berg, E.J., Younesi, R. (2022) The Role of EC and Sulfolane on the Dissolution of Transition Metals from Lithium-Ion Cathodes. *Submitted*

VI. **<u>Tesfamhret, Y.</u>**, Liu, H., Berg, E.J., Younesi, R. (2022) Investigation of the Effect of Lithium Difluoro Phosphate Electrolyte Additive on Transition Metal Dissolution from High Voltage Cathodes. *In manuscript*

My contribution to the papers

I. Planned the project together with my supervisors. Performed all experiments. SEM and XPS characterizations were performed together with H. Liu. Processed data and wrote manuscript with input from co-authors.

II. Planned the thin film part of the project together with co-authors. Performed ALD deposition and ICP characterisation. Wrote the related experimental details, took part in general discussions and gave feedback on the manuscript.

III. Planned the thin film part of the project together with co-authors. Performed ALD deposition and ICP characterisation. Wrote the related experimental details, took part in general discussions and gave feedback on the manuscript.

IV. Planned the project together with my supervisors. Performed all experiments. Processed data and wrote manuscript with input from co-authors.

V. Planned the project together with my supervisors. Performed all experiments. Processed data and wrote manuscript with input from co-authors.

VI. Planned the project together with co-authors. Performed all experiments. XPS characterization was performed together with H. Liu. Processed data and wrote manuscript with input from co-authors.

Disclaimer: Parts of this thesis are based on my licentiate thesis titled *On the dissolution of transition metals from cathode materials* (Uppsala University, 2021). Reprints were made with permission from the respective publishers.

Papers not included in the thesis:

- Chai, Z., Mattsson, A., **<u>Tesfamhret, Y.</u>**, Österlund, L., Zhu, J., (2020) Ni-Ag nanostructure-modified graphitic carbon nitride for enhanced performance of solar-driven hydrogen production from ethanol. *ACS Applied Energy Materials*, 3(10):10131–10138

- **<u>Tesfamhret, Y.</u>**, Carboni, M., Asfaw, H.D., Kullgren, J., Younesi, R. (2021) Revealing Capacity fading in Sb-based anodes using symmetric sodium-ion cells. *Journal of Physics: Materials*, 4(2):024007

- Sailan, G.D., Højberg, J., Elkjær, C.F., **<u>Tesfamhret, Y.</u>**, Hernández, G., Lacey, M.J., Younesi, R. (2022) Investigation of Water-Soluble Binders for $LiNi_{0.5}Mn_{1.5}O_4$-Based Full Cells. *ChemistryOpen*, 169(1):010530

Contents

Abbreviations

ADF	Annular dark-field
AEDB	2-aminoethyldiphenyl borate
ALD	Atomic layer deposition
BET	Brunauer–Emmett–Teller
CDTA	(1,2-Cyclohexylenedinitrilo)tetraacetic acid
CE	Coulombic efficiency
CEI	Cathode electrolyte interphase
DEC	Diethyl carbonate
DFT	Density functional theory
DMC	Dimethyl carbonate
EC	Ethylene carbonate
EDS	Energy-dispersive X-ray spectroscopy
EELS	Electron energy loss spectroscopy
EMC	Ethyl methyl carbonate
FB	Fluidized bed
FEC	Fluoroethylene carbonate
GHG	Greenhouse Gas
HADAAF	High angle annular dark-field
HCP	Hexagonal closed packed
HOMO	Highest occupied molecular orbital
ICP	Inductive coupled plasma
IEA	International Energy Agency
ISE	Ion selective electrode
KF	Karl Fischer
LCO	Lithium cobalt oxide
LDR	Linear dynamic range
LFP	Lithium iron phosphate
LIB	Lithium ion battery
LiBOB	Lithium bis(oxalato)borate
LiDFP	Lithium difluorophosphate
LMO	Lithium manganese oxide
LNMO	Lithium nickel manganese oxide
LNO	Lithium nickel oxide
LUMO	Lowest unoccupied molecular orbital
MS	Mass spectrometry

NiMH	Nickel-metal hydride
NMC	Lithium nickel manganese cobalt oxide
OCV	Open circuit voltage
OES	Optical emission spectroscopy
PBF	Pyridine boron trifluoride
PC	Propylene Carbonate
PES	Prop-1-ene-1,3-sultone
PFO-EC	Perfluorooctyl-substituted ethylene carbonate
PITT	Potentiometer intermittent titration technique
QCM	Quartz crystal microbalance
RF	Radio-frequency
SEI	Solid electrolyte interphase
SEM	Scanning electron microscopy
SL	Tetramethylene sulfone
SOC	State of charge
STD	Standard deviation
STEM	Scanning transmission electron microscopy
TBAF	Tetra-n-butylammonium fluoride
TEM	Transmission electron microscopy
THF	Tetrahydrofuran
TISAB	Total ionic strength adjustment buffer
TM	Transition metal
TMA	Trimethylaluminum
TMSPa	tris-(trimethylsilyl)phosphate
TMSPi	tris-(trimethylsilyl)phosphite
VC	Vinylene carbonate
XPS	X-ray photoelectron spectroscopy
XRD	X-ray diffraction

1 Introduction

1.1 Energy revolution

As economic activity has increased over the last several decades, conventional energy sources (fossil fuels) have become the primary causes of air pollutants such as CO_2, CH_4 and N_2O.[1] The rapid rise of greenhouse gas (GHG) emissions in the natural environment has radically altered global temperatures while posing new hazards to human health and other sectors such as agriculture. According to the International Energy Agency (IEA), the share of new generation fuel and renewable energy is growing due to the fast development of a secure and sustainable energy system with net-zero emissions.[2] The Kyoto and Paris agreements set a minimal target of significantly reducing emissions into the atmosphere from fossil derived energy resources by 2060. The 195 countries committed to keep global temperature rises well below 2 °C above the pre-industrial levels of 1750.[3] It is anticipated that human activities have already caused around 1.0 °C of global warming over pre-industrial levels, and it is projected that this will reach 1.5 °C before 2050, if the rise continues at the present pace.[3] To make the agreement goal a reality, there must be a significant shift in how energy is harnessed and used internationally. This goal can only be met by incorporating renewable sources such as solar, wind, *etc*. Renewable energy options that are substitute alternatives to traditional fossil fuel-based energy sources are currently disadvantaged by intermittency and should thus be accompanied by an adequate energy storage system. The most common energy storage device for power system applications is battery technology. Battery energy storage applications include electric grids, transportation, marine and submarine operations, aeronautical operations, portable electronic devices, and wireless network systems, to name a few. The battery, as an energy storage system, seems to regularly provide a solution to every imperative question it has faced. Yet, to satisfy future standards and demands of the growing global economy, constant evolution of the currently commercialized and forthcoming battery variations is critical.

1.2 Lithium-ion batteries

A battery is a device that converts chemical energy by means of an electro-chemical reduction-oxidation (redox) reaction into electrical energy. There are two types of batteries generally available: primary and secondary. The electrode reactions in primary batteries are not reversible, and thus the battery cells are not rechargeable. The electrode reactions in secondary/rechargeable batteries, however, are reversible. An applied electrical energy reverses the battery's operation, restoring charge. Li-ion batteries (LIBs) are prime secondary battery examples that have dominated the individual market since their commercial introduction in the 1990s.[4] LIBs have been the go-to candidates owing to their collective characteristics of relatively high gravimetric and volumetric energy density as well as long-term stability compared to several other battery chemistries. LIBs are typically made up of two electrodes coupled by both an electrolyte component that is ionically conductive and an external electric circuit, as illustrated in Figure 1.1. The cathode is defined as the electrode in which a reduction-reaction occurs (*i.e.* electrons are taken from the external circuit) during the discharge, while at the anode ensues an oxidation-reaction (*i.e.* electrons are donated to the outer circuit) at the same time. The electrolyte is a component that is electronically insulating, but a strong conductor of ions. At room temperature, the ionic conductivity of commonly used non-aqueous electrolytes can exceed 10 mS/cm.[5] The key purpose of the electrolyte is to provide a medium for ion transport and charge compensation. It allows working ions (from the salt containing them) to be transported from one electrode to another. It also prevents short-circuiting by acting as a physical barrier between the electrodes, either alone if the electrolyte is solid, or immersed in a solid matrix (the separator) if it is liquid.
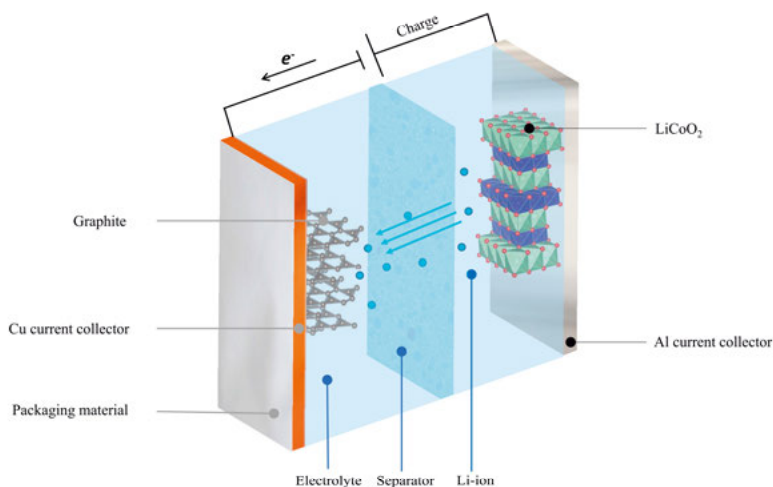
Figure 1.1. A schematic of $LiCoO_2$ vs. graphite lithium-ion electrochemical cell.

Although young relative to competing technologies, *e.g.*, nickel-metal hydride (NiMH) and alkaline batteries, the LIB technology is based on an extensively researched and developed chemistry that has resulted in a diverse range of electrode materials for both positive (*e.g.,* $LiCoO_2$, $LiMn_2O_4$, $LiFePO_4$, *etc.*) and negative electrodes (*e.g.,* C, Sn, Si, *etc.*). Thermodynamics define the fundamental properties of a battery, such as the equilibrium voltage and the storage capabilities (capacity). The electrochemical potential of a cell (E_{cell}), *i.e.* the difference in redox reaction potentials of the active materials in the electrodes, is related to the Gibbs free energy (ΔG) of the redox reaction as follows;

$$\Delta G = -nFE_{cell} \tag{1.1}$$

where *n* is the number of moles of electrons exchanged in the reaction and *F* is Faraday constant, *i.e.* the amount of charge carried by one mole of electrons. ΔG signifies the maximum amount of work that can be performed during a chemical reaction.[6] The theoretical capacity (C_t) of electrode materials is proportional to the number of electrons in the reaction and the molar weight of the chosen materials, as stated by the following equation;

$$C_t = \frac{nF}{3.6 \times M} \tag{1.2}$$

where *M* is the molar mass of the active material. The number of Li-ions accommodated in the active materials host lattice correlates directly with the quantity of electrons.[6] The equation suggests that, in principle, a higher capacity may be achieved by a decreased molecular weight and the accommodation of more electrons per formula unit.

1.3 The LIB Cathode

Cathode materials based on transition metal oxides and their derivatives have sparked significant interest in both research and commercial applications since the introduction of $LiCoO_2$ (LCO).[7] After more than four decades, the layered LCO first developed by Goodenough *et al.* continues to be one of the most commonly used cathode materials.[8] The layered oxide structure of LCO can be described by the R($-$)3m space group with Li and Co cations in alternating layers occupying octahedral positions formed by the fcc close-packed lattice of oxygen anions (<u>Figure 1.2</u>). LCO with the redox couple centre Co^{3+}/Co^{4+} has a capacity of 140 mhA/g in the range of 3 V – 4.2 V *vs.* Li/Li^+ and is easy to synthesise due to the large ionic radius difference between Li^+ (0.76 Å) and Co^{3+} (0.545 Å). The cut-off voltage of 4.2 V *vs.* Li/Li^+ corresponds to approximately half of the delithiation capacity of the material (*i.e.* $Li_{0.5}CoO_2$).[9] However, delithiating LCO to $E > 4.2$ *vs.* Li/Li^+ causes irreversible structural

changes, Co dissolution, and significant volume changes.[10,11] Concerns have also been raised regarding the future of LCO because of its limited practical capacity, thermal instability, reported price hikes for cobalt and cobalt minerals, and ethical considerations regarding the mining and outsourcing of Co.[12,13] Since Ni is more abundant, $LiNiO_2$ (which is isostructural and has similar practical capacity as LCO) has also been explored.[14] However, $LiNiO_2$ has been reported to be difficult to synthesize and to have a tendency for Ni-ions to replace Li^+ during delithiation (cation mixing), obstructing Li^+ diffusion and resulting in severe structural degradation.[15–18] Due to the lower cost and lower toxicity of Mn, $LiMnO_2$ with the identical structure also attracts interest.[19] However, the structural instability of the layered structure and the dissolution of Mn during electrochemical cycling continue to hamper the material's commercialization.[20] Ohzuku *et al.* introduced the electrochemical application of mixed transition metal oxides, also termed NMC ($LiNi_xCo_yMn_zO_2$, where x + y + z = 1), which offers ~150 mAh/g at 4.2 V *vs.* Li/Li^+.[21] The relative concentrations of Ni, Mn, and Co in the structure can be changed to take advantage of each transition metal. Depending on the TM ratios in the structure, the redox couples Ni^{2+}/Ni^{3+} and Ni^{3+}/Ni^{4+} contribute to the majority of the capacity, with Co^{3+}/Co^{4+} also participating. Mn-rich NMC are more thermally and structurally stable, but their capacities are reduced due to the electrochemical inactivity of Mn^{4+} (Figure 1.3).[22] Co-rich NMC improve electronic conductivity and thus also rate capability and moreover decrease cation disorder.[23]
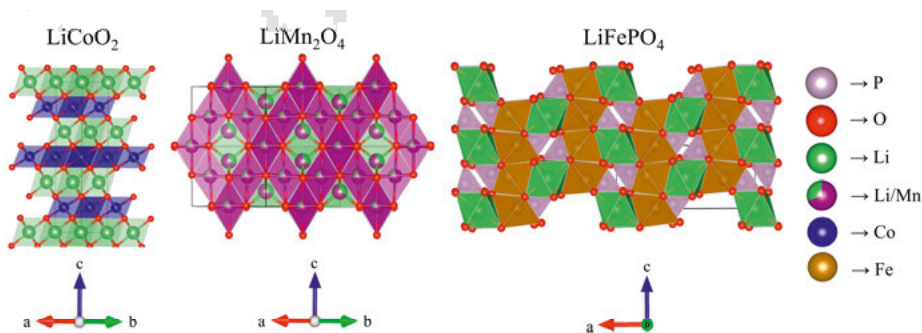

Figure 1.2. Layered oxide LCO, spinel LMO and Olivine LFP crystal structures.

Of the mixed TM layered oxides, Ni-rich NMC has recently gained the most interest due to the possibility of achieving a practical capacity of above 200 mAh/g when delithiated to $E > 4.6$ V *vs.* Li/Li^+.[24,25] They are also appealing due to the reduction of the problematic Co and inactive Mn. Ni-rich NMC, on the other hand, have their own set of issues, such as cation mixing (due to the similar radius of Ni^{2+} and Li^+), crack formation, and the highly reactive Ni^{4+} participation in electrolyte degradation mechanisms, to name a few.[26] Similar cathodes in the form of $LiNi_{1-x-y}Co_xAl_yO_2$ (1-x-y $\geq$ 0.8, NCA) are also widely used in commercial applications. However, similar ageing mechanisms prevent the

full exploitation of the theoretical capacities that the mixed TM layered oxides can offer.[27]
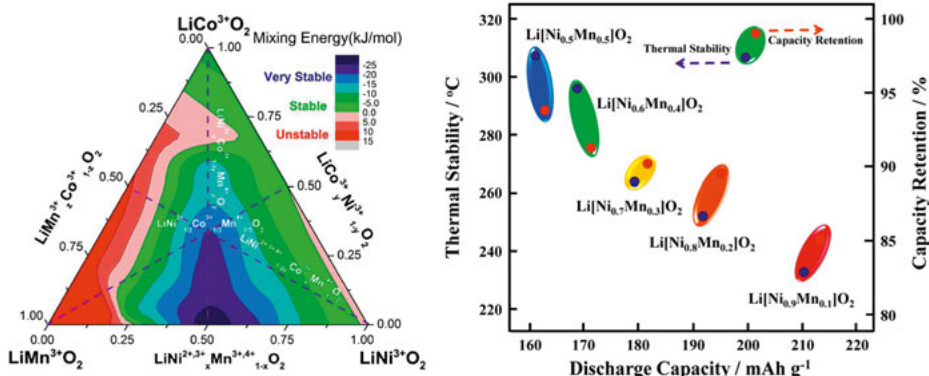

Figure 1.3. (a) Phase triangle on the stability of TM-oxide solid solutions, LiTMO$_2$ (TM = Ni, Co, Mn), Reproduced with permission from reference [28]. (b) A map of relationship between discharge capacity, thermal stability and capacity retention of Li/Li[Ni$_x$Co$_y$Mn$_z$]O$_2$ (x = 1/3, 0.5, 0.6, 0.7, 0.8 and 0.85). Reproduced from reference [29] with permission.

Over three decades ago, Thackeray *et al.* introduced spinel LMO (LiMn$_2$O$_4$) as a cathode material. The above mentioned advantages of Mn selection, as well as the ease of production and low cost of the cathode material, made spinel LMO a viable option.[30] LMO, which has a spinel crystal structure with the space group Fd3m, provides a three-dimensional conduit for Li$^+$ migration during electrochemical cycling, resulting in a good rate capability. In the cubic spinel structure of LMO, a close-packed oxygen array allocates cations to octahedral and tetrahedral positions.[31] The octahedral sites are occupied by a stoichiometrically equal amount of Mn^{3+} and Mn^{4+}, while lithium occupies the tetrahedral sites.[32] LMO provides 148 mAh/g when using the cut-off voltage of 4.3 V *vs.* Li/Li$^+$. Spinel LNMO (LiNi$_{0.5-x}$Mn$_{1.5+x}$O$_4$), an isostructure of LMO in which Ni typically accounts for 25% of the TM, is another promising cathode material due to its high average operating voltage (4.7 V *vs.* Li/Li$^+$). LNMO has an energy density comparable to Ni-rich cathodes; however, such operating voltages necessitate electrolytes with greater thermodynamic stability. Polyanionic compounds, most notably LFP (LiFePO$_4$), are also commercially available. Owing to the intrinsic stability of the PO$_4^{3-}$ polyanion group, LFP offers relatively high thermal and general cycling stability. Li$^+$ and Fe-ions are situated in octahedral positions inside the olivine structure of LFP, whereas P occupies tetrahedral positions within a hexagonal close-packed (HCP) oxygen arrangement.[33] Although LFP has a practical capacity of 150 mAh/g, the material's low electronic conductivity and relatively low operating voltage limit its predominant use.

1.4 Electrolyte

When the redox potential of the electrodes in an electrochemical cell exceeds the electrochemical stability window of the electrolyte, an interphase layer composed of electrolyte degradation products may develop. The electrochemical stability window of the electrolyte is defined by the energy gap between the highest occupied molecular orbital (HOMO) and the lowest unoccupied molecular orbital (LUMO), as shown in Figure 1.4. The anode and cathode must be chosen so that the electrochemical potential of the anode is lower than the LUMO and the electrochemical potential of the cathode is higher than the HOMO; otherwise, the electrolyte will be reduced on the anode or oxidized on the cathode, forming a passivating cathode electrolyte interphase (CEI) or solid electrolyte interphase (SEI), respectively.

Commonly used and commercially available LIB electrolytes are combinations of alkyl carbonates containing ethylene carbonate (EC) solvent as an important component for sufficient negative electrode passivation, combined with dimethyl, diethyl, or ethyl-methyl carbonate co-solvents (DMC, DEC, EMC, respectively). The operating potentials of the majority of cathode and anode materials mentioned in the previous section depart slightly from the thermodynamic stability window of carbonate electrolytes. The SEI or CEI serve as a physical barrier that inhibits electrolyte degradation and electrode corrosion by preventing direct contact between the electrolyte and electrode materials. Therefore, mechanical, chemical, and electrochemical stabilities of these layers play crucial roles in influencing the performance and stability of the cell. During electrochemical reactions, mechanical volume changes can reach up to 10-20 % (excluding alloy and conversion types, which display higher values) in electrode materials.[34,35] This undesired characteristic thus necessitates certain important characteristics from the electrode/electrolyte interfaces. An ideal electrode/electrolyte interfacial layer should be an electrical resistor, a good ionic (Li^+) conductor, be homogenous in morphology (for uniform current distribution), and mechanically stable and flexible (to manage volume changes).[36–39] However, because the formation of these layers is a direct result of electrolyte and electrode surface degradation, including the loss of active Li^+, an efficient layer formation is critical. In addition, due to their high polarity, temperature range of operation, and limited toxicity relative to other solvent types, carbonate electrolytes have been preferable candidates so far.[40] Some alternative notable electrolyte solvents are ether-based electrolytes that have a high affinity for Li-metal anode, but are unstable over 4 V *vs.* Li/Li^+.[41] Sulfone-based solvents have a large dielectric constant (>40) and a high oxidation potential (>5 V *vs.* Li/Li^+), demonstrating stability with high-voltage cathodes.[42] However, the wettability and compatibility of sulfone-based solvents with Li-metal and graphite anodes is poor.[43]

LiPF$_6$ is the most frequently used LIB electrolyte salt, which is somewhat of a compromise and chosen as the lesser of all evils. The competing salts have far greater drawbacks. Due to the explosivity of LiClO$_4$ as a result of its highly oxidative qualities, the toxicity of LiAsF$_6$, the unfavourable behaviour of LiBF$_4$ or LiBOB with respect to passivation of the anode surface, and the low conductivity of LiSO$_3$CF$_3$, LiPF$_6$ is still a suitable option for commercialization and benchmark studies.[44,45] Some advantages of LiPF$_6$ include sufficient solvation concentrations in the aforementioned carbonate electrolytes, good ionic conductivity and passivation of the aluminium current collector of cathodes to prevent corrosion.
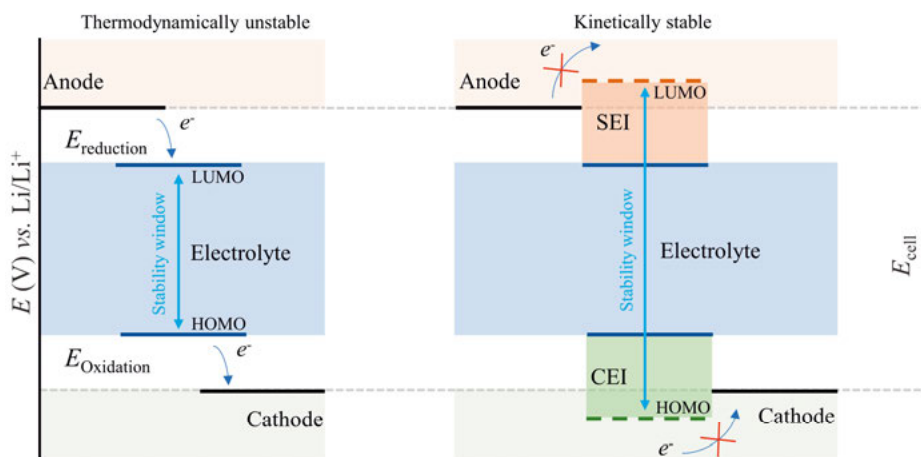

Figure 1.4. An illustration of a thermodynamically unstable (left) and kinetically stable (right) electrolyte. Illustration drawn with inspiration from references [46] and [47].

1.5 Cathode/electrolyte interphase

The specific capacity (Q) of the electrode materials and their difference in electrochemical potential (E_{cell}) are the two main parameters that define the energy density (U) of a battery.

$$U = Q \times E_{cell} \qquad (1.3)$$

In current LIB technology, cell voltage and capacity are mostly dictated by cathode materials. LIB energy densities are hampered by the limited specific capacity of the cathode materials, relative to typical anodes such as graphite (372 mAh/g) and Si (4200 mAh/g). Furthermore, as the anode materials already operate at an average potential close to metallic lithium (*e.g.*, graphite at $E \sim$ 0.2 V *vs.* Li/Li$^+$), increasing the total voltage of the battery depends on increasing the average working potential of cathode materials. Therefore, increasing the average operating potential of existing cathodes is critical in order to reduce the weight, and thereby cost of various battery applications.

A lot of effort has gone into developing high voltage cathode materials such as Ni-rich layered oxides and LNMO. When attempting to achieve increased energy density, the *first* challenge that must be addressed is the *structural integrity* of the high voltage cathodes in a charged state. As mentioned in **section 1.3**, Ni is incorporated as a redox active centre to maintain increased capacity, whereas the inclusion of inactive and structural Mn improves thermal stability and, consequently, safety in Ni-rich NMCs. During delithiation of the cathode materials, Co and Ni are oxidized to +IV. When these species come into contact with the electron-rich species in the cathode/electrolyte interphase, they undergo irreversible reduction, which is problematic. These reduction reactions cause electrolyte decomposition, as well as surface structural reconstruction from the original layered structure to a spinel and/or rock-salt-like phases, which is rich in Co^{2+} and Ni^{2+}.[26,48] Similarly, spinel TM-oxide surfaces undergo thermodynamically driven structural reconstruction. Delithiated spinels such as those of LMO and LNMO have also been found to generate 'Mn$_3$O$_4$-like' or rock-salt-like phases near the surface.[49,50] The formation of a less electronically conductive rock salt structure increases the barrier for Li$^+$ hopping, creating kinetic limits into the electrochemical process and thus resulting in an increased cathode impedance.[51] In addition, the formation of cracks and the evolution of oxygen due to cathode surface internal stresses result in newly exposed surfaces that provide additional locations for CEI formation.[52] The release of reactive oxygen (O^{2-}) from the TM-oxide surface increases electrolyte degradation and contributes to the formation of TM leaching agents (such as HF). Multiple studies have shown that the onset E for oxygen release correlates well with the onset of CO and CO$_2$ evolution driven by irreversible electrolyte degradation.[53]

This brings us to the *second* challenge to be addressed in attempting to achieve high voltage performance: the chemical and electrochemical *stability of organic carbonate-based electrolytes*, which are frequently coupled with high voltage cathodes. The low anodic stability of "standard" carbonate-based electrolytes makes development of high-voltage cells extremely challenging. Multiple studies have investigated the complicated interactions of metal-oxides with carbonate solvents and common Li-salts. Among the proposed mechanisms for electrolyte oxidative degradation mechanisms are nucleophilic attack reactions involving oxides and carbonate molecules, electrophilic attack, and dehydrogenation processes.[54]

Azarate *et al*. demonstrated that the electrochemical oxidation of EC:DMC electrolyte in the presence of $LiPF_6$ salt, coupled by proton transfer to salt anions or other solvent molecules, can be expected already at 4.2 V *vs*. Li/Li^+.[55] However, the onset E may vary based on the type and ratio of carbonate solvents and the type and concentration of salt. Yu *et al*. proposed a decomposition mechanism of EC solvent and $LiPF_6$ salt upon oxidation in the presence of TM-oxide, in which EC molecules dissociate on the oxide surface, forming dehydrogenated species and surface protic species.[54] Depending on the oxide chemistry, the predicted chemical decomposition of the electrolyte on the oxide surface begins approximately at 4.1-4.8 V *vs*. Li/Li^+. Zhang *et al*. also reported, based on DFT calculations, that this mechanism of EC degradation on the cathode surface oxygen is the most energetically favourable mechanism (Figure 1.5).[56] The protic species on the metal oxide surface may also attack PF_6^- anions, resulting in acidic species such as HF. Since oxidative degradation of solvent also leads to degradation of salt, the acid-base reactions resulting from the presence of HF in electrolyte solutions containing $LiPF_6$ salt are particularly pertinent cathode ageing processes.[57] Increased temperature facilitates the propagation of this process, resulting in increased deterioration of the cathode surface and TM dissolution, implying that the mechanism is chemical as well as being initiated indirectly by electrode potential. The prototypical carbonate solvents such as DEC, propylene carbonate (PC), DMC or EMC, have also been shown to undergo similar oxidative degradation mechanisms to EC, although to a lower extent.[48,58,59] The cathode/electrolyte interaction is quite complex and highly dependent on surface area of the studied cathode materials and the corresponding chemistry of cell components. Therefore, controlling the aforementioned ageing mechanisms or developing an efficient CEI also becomes complex.
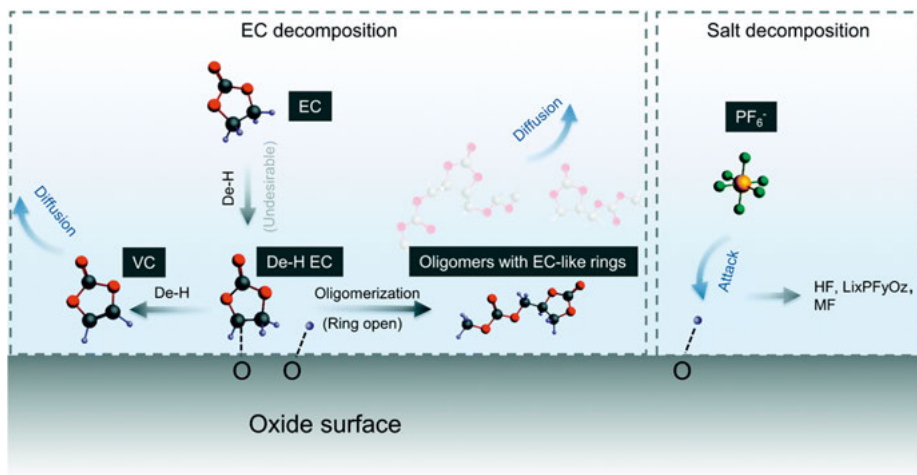
Figure 1.5. Electrolyte decompositions on TM-oxide surface. Electrolyte decompositions include solvent (EC) decomposition and coupled salt (PF_6^-) decomposition. Solvent decomposition occurs by dehydrogenation first, and 'de-H' EC could be further decomposed by removing another hydrogen or by oligomerization. The protic species on the surface coming from dehydrogenation could further attack PF_6^- and lead to coupled salt decomposition. Figure reproduced with permission from reference [56].

1.6 Transition metal dissolution

The degradation mechanisms discussed in the **section 1.5** partly lead to formation of acidic species, in the presence of salt anions. These acidic species can be quite corrosive towards the cathode surface. Decomposition reactions that result in TM dissolution lead to a direct loss of redox active material as well as migration and deposition of the TM on the anode surface, which not only alters the cathode surface structure but also induces impedance and negatively affects cyclability (Figure 1.6).[60,61] Klein *et al.* have, among others, shown that cumulative TM deposition at the anode correlates to the formation of Li-metal dendrites.[62] This process will eventually end in the loss of active lithium, as well as failure due to short circuit.[63] Furthermore, Mn^{2+} has been shown to penetrate the SEI and remain in the inner area between the SEI and the anode by exchanging places with Li^+ ions.[64] The presence of TM-containing species in the SEI impedes Li^+ transport.[65] Furthermore, the recurring generation of C_2H_4 from SEI has demonstrated that Mn^{2+} is detrimental to both solvents and graphite anodes, acting as a catalyst and propagating further reactions, resulting in thicker SEI.[66] Wang *et al.* also examined effects of Mn-ions in the bulk electrolyte, and suggested that Mn^{2+} destabilize electrolyte components due to its peculiar solvation-shell structure, which catalyses the decomposition of carbonate molecules and PF_6^- anion.[67]

This dissolution phenomenon has been reported to be particularly pronounced in spinel-LMO and spinel-LNMO. Mn dissolution from LMO has been primarily explained by; (i) charge disproportionation reactions and (ii) subsequent corrosion due to increased electrolyte acidity.[68–73] The charge disproportionation reaction, which is induced by Mn^{3+}, results in Mn^{4+} and Mn^{2+}.[74,75] whereby the Mn^{2+} species proposedly display higher solubility in the electrolyte. The common conception of Mn^{2+} dissolution however comes from the observations of Mn^{2+} in the electrolyte and/or deposited on the anode surface. A mechanism induced by reductive coupling ($TM^{4+} + O^{2-} \rightarrow TM^{2+} + O$) of TMs at the oxide surface with loosely bound oxygen could elucidate the lower oxidation state that is observed. There are also other factors controlling TM dissolution. Tarascon *et al.* reported the inferior cyclability of LMO at elevated temperatures.[76] Furthermore, Shizuka *et al.* and Bhatia *et al.* along with others have since shown that the dissolution of Mn-ions from LNMO and LMO is particularly increased at higher state of charge.[70,71,77–80] In delithiated state, however, Mn should mostly be in +IV state, contradicting a dissolution process primarily initiated by disproportionation.[34–37]

Mn dissolution has also been observed in mixed TM layered oxides (NMC), which contain only structural inactive Mn^{4+}, indicating that the commonly used disproportionation process is unlikely.[60,81] A hypothesis that has been suggested as the root cause is 'acid attack'. As described in **section 1.5**, acidic species in the electrolyte increase due the electrolyte degradation. Therefore, there likely exists an acid-base electrolyte-cathode interaction that results in TM dissolution. In general, TM dissolution has been reported to accelerate at, (i) high SOC, (ii) increased temperature, (iii) increased presence of electrolyte degradation products.
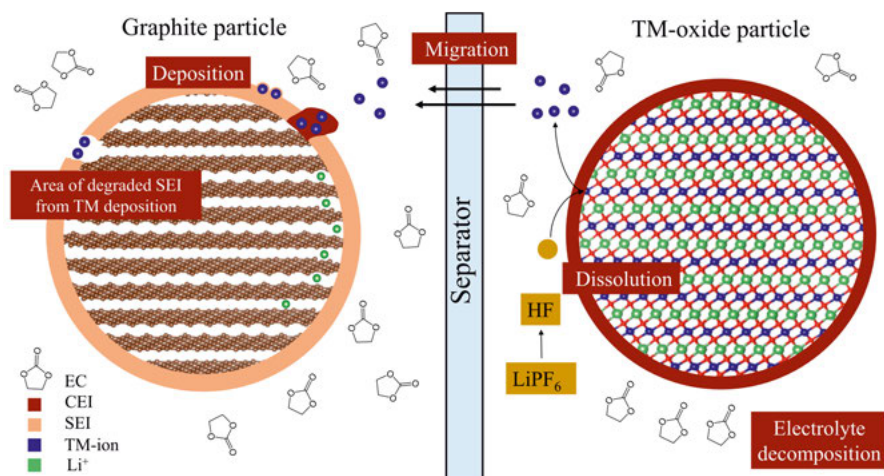

Figure 1.6. Schematic showing the various consequences and causes of transition metal dissolution, including the link with both SEI and CEI formation and growth. Illustration redrawn based on inspiration from reference [82].

1.7 Mitigation of transition metal dissolution

Since TM dissolution is a direct consequence of cathode/electrolyte interaction, the surface chemistry and thereby also surface area of the cathode is an important parameter. To mitigate this mechanism, many approaches have been presented in the literature. The strategies may be divided into two main categories;

1.7.1 Optimizing the cathode/electrolyte interphase

Coating the surface of a cathode with electronically insulating components has long been adopted as a strategy to stabilize its electrochemical properties. These coatings are designed to act as an electronic barrier to direct contact between electrolyte and redox-active TM-ions in the oxide surface. In addition, the coatings act as a sacrificial layer to the acidic environment that the electrolyte provides. Including a layer of such properties may introduce impedance increase due to lower electronic contact of the cathode particles. Although this approach has led to improvements in durability of high voltage cathodes, complete passivation against deleterious irreversible processes has not yet been achieved. Furthermore, typical coatings are not well-matched to the atomic structure of the active materials. The structural mismatch between bulk and surface gets aggravated by the volume changes undergone by the cathode during cycling. Furthermore, the difficulty of achieving uniform and conformal as well as ultrathin coatings in highly porous materials has made this approach especially difficult to generalize and very cathode material-specific.

Many coatings techniques have been suggested in literature to mitigate cathode ageing, but the most optimum results are obtained using atomic layer deposition (ALD). ALD is recognized for its conformal nature and for the relatively uniform nature of the produced films, resulting in minimal pinholes or thickness variations when compared to techniques such as sol-gel, wet-chemical coating, acid solid state sintering, *etc*. Thin film coatings can be in the form of metal-oxides, -fluorides and -phosphates.[24,83,84] Numerous cathode materials have been employed as coating layers to stabilize cathode surfaces, such as Al_2O_3, TiO_2, ZrO_2, Bi_2O_3, ZnO, $AlPO_4$, AlF_3 and so on.[66,85–87] The commonly applied Al_2O_3 and TiO_2 films will be discussed in this thesis.

Another strategy that has a direct impact on the cathode/electrolyte interphase is the implementation of an additive in the electrolyte. Flouroethylene carbonate (FEC), vinyl carbonate (VC), tris(trimethylsilyl) phosphite (TMSPi), tris(trimethylsilyl)phosphate (TMSPa), prop-1-ene-1,3-sultone (PES), pyridine boron trifluoride (PBF), 2-aminoethyldiphenyl borate (AEDB), and polyfluoro-alkyls (4-(perfluorooctyl)-1,3-dioxolan-2-one, PFO-EC) and much more have been proposed as electrolyte additives.[88–93] The use of suitable electrolyte additives is a strategy that offers a techno-economic benefit and is commonly used to achieve the formation of optimum CEI and/or SEI, to mitigate ageing.

TMSPi and TMSPa have been demonstrated to show their HF scavenging ability, which reduces electrolytes acidity and thereby cathode corrosion. Lithium difluorophosphate (LiDFP) has been shown to scavenge already dissolved TM-ions thus reducing the rate of dissolved TM from depositing on the anode surface. LiDFP is an additive that will be discussed in this thesis. Generally, the fundamental idea of an additive in the electrolyte is the modification of either CEI or SEI or both, to stabilize the interfacial interaction of electrode/electrolyte. The replacement of electrolyte co-solvents such as EC with high anodic stability solvents such as sulfone-based solvents is also a strategy that has seen a room for improvement, and will also be discussed in this thesis.

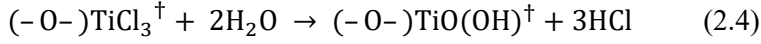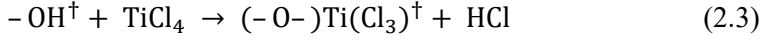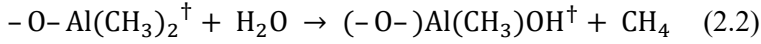## 1.7.2 Optimizing the cathode bulk structure

The electrochemical performance of cathode materials is also determined by the physical properties of the precursors and the method of synthesis. Various synthesis approaches have been proposed, including co-precipitation, sol-gel method, solid-state reaction, and spray drying method, *etc*.[33,94] The investigation and development of these synthesis pathways has mostly focused on determining how to regulate particle size, minimize cost, and enhance electrochemical characteristics. Although these properties are not addressed in this thesis, below are several synthesis-based cathode optimization strategies that can help to reduce cathode ageing and thereby TM dissolution. Doping is a straightforward approach that employs atomic-scale lattice modification which uses non-intrinsic ions as doping elements in the oxide structure to address structural and thermal instability. For example, in Ni-rich NMC, Ni and Mn on the surface may be preferentially substituted by cations/anions during synthesis to suppress corrosion by acidic species in the electrolyte. Liang *et al*. showed that doping Zr or Ti at the Co site and doping Al at the Mn site is suitable for NMC811 in solid state synthesis.[95] Park *et al*. demonstrated Boron ions as dopants to modify the surface energy of cathode, resulting in a highly micro-structured material that can somewhat alleviate the inherent internal strain of the Ni-rich NMC cathode during the lithiation/de-lithiation processes.[96] Anion doping suggests a process in which halide ions exchange places in the neighbourhood of Li and Ni ions, resulting in a more stable local halide octahedron. When F substitutes the oxygen site in Ni-rich NMC, the local valence balance is disrupted, leading to a higher negative charge near O and a less positive charge near Ni, which contributes to a structure more conducive of Li^+.[97] Similarly, the crystalline phase of LMO can be stabilized by bulk and surface metal ion dopants that typically have an oxidation state lower than +III, such as Al^{2+}, Co^{2+} and Ti^+.[98–100] The average valence of Mn is thus kept higher than +3.5, resulting in a lower Mn^{3+} content in LMO. By decreasing the amount of Mn^{3+}, which is susceptible to charge disproportionation, Mn dissolution is correspondingly decreased. However, this strategy only considers disproportionation of Mn^{3+} as the lead cause of TM dissolution. The stabilization of cathode surface through doping,

however, should reduce the surface reconstruction experienced from the mentioned TM-oxide cathodes, thereby reducing the oxygen release. Core-shell TM concentration gradient optimization of NMC has also been explored in studies, as a synthesis-based strategy.[101]

2 Methods

2.1 Atomic Layer Deposition

Atomic layer deposition (ALD) is a film deposition technique that is able to meet the requirements for atomic layer controlled and conformal depositions, due to its sequential and self-limiting surface reactions. <u>Figure 2.1</u> illustrates the parallel and self-limiting surface reactions that take place during ALD deposition. The majority of ALD depositions are based on binary reaction sequences in which two surface reactions result in a binary compound film. As there is a limited number of surface sites, the reactions can only deposit a limited number of surface species. If the two surface reactions are self-limiting, the reactions can continue depositing a thin film while maintaining atomic-level control. The advantage of ALD is its ability to precisely control thickness in Ångström or monolayers levels. On structures with high aspect ratios, the self-limiting characteristic of ALD enables excellent phase coverage and conformal deposition. Due to numerous precursor gas fluxes, some surface regions will react prior to others. However, the precursors will adsorb and eventually desorb from the areas of the surface where the reaction has been completed. The precursors will then begin to react with other unreacted surface areas to produce a conformal deposition. ALD is attractive for industrial applications since it can be applied to very large substrates as well as multiple substrates that are processed simultaneously. Although ALD precursors can be in gas, liquid, or solid form, precursor molecules are introduced in gas phase to ensure complete coverage of the substrate regardless of its geometry and without the need for a direct line-of-sight.[102] In this regard, scaling up ALD is limited by the size of the reaction chamber, in addition to the kinetic and thermodynamic aspects of the reactions. Since reactants in the gas phase are not in contact, surface reactions occur in sequence. This separation of the two reactions reduces the likelihood of gas-phase reactions between the various precursor molecules, which can generate particles that can be deposited to form granular surface films. In this thesis, Al_2O_3 and TiO_2 were deposited by ALD. Trimethylaluminum (TMA) and H_2O were used as precursors for Al_2O_3. $TiCl_4$ and H_2O were used for TiO_2. The precursors undergo the following reactions on the substrate/cathode.[103,104]

$$- \, \text{OH}^{\dagger} \, + \, \text{Al(CH)}_3 \; \rightarrow \; (-\text{O}-)\text{Al(CH}_3)_2{}^{\dagger} \, + \, \text{CH}_4 \qquad (2.1)$$

$$- \, \text{O}-\text{Al(CH}_3)_2{}^{\dagger} \, + \, \text{H}_2\text{O} \; \rightarrow \; (-\text{O}-)\text{Al(CH}_3)\text{OH}^{\dagger} \, + \, \text{CH}_4 \quad (2.2)$$

$$- \, \text{OH}^{\dagger} \, + \, \text{TiCl}_4 \; \rightarrow \; (-\text{O}-)\text{Ti(Cl}_3)^{\dagger} \, + \, \text{HCl} \qquad (2.3)$$

$$(-\text{O}-)\text{TiCl}_3{}^{\dagger} \, + \, 2\text{H}_2\text{O} \; \rightarrow \; (-\text{O}-)\text{TiO(OH)}^{\dagger} \, + \, 3\text{HCl} \qquad (2.4)$$
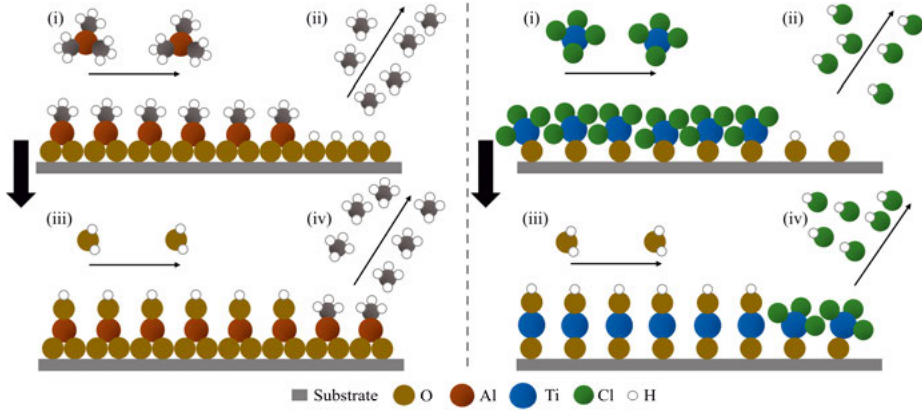
†surface species

Figure 2.1. An illustration of Al_2O_3 (left) and TiO_2 (right) ALD deposition. Notice that the ratios of the atom size illustration are inaccurate.

During ALD deposition, the substrate is alternately exposed to TMA/TiCl$_4$ and H$_2$O. The formation of a very tight Al–O or Ti–O bond is the driving force for effective reactions. Al$_2$O$_3$ growth is highly linear with the number of cycles when surface reactions are repeated. The average growth rates of Al$_2$O$_3$ and TiO$_2$ are estimated to be ~1.1-1.3 Å and ~0.6 Å per cycle, respectively.[100,105] A single ALD cycle produces far less growth than a single "monolayer" of Al$_2$O$_3$ and TiO$_2$. Thus, the growth rate of each cycle can be compared to the thickness of one monolayer with the respective oxide coating. To prevent the interdiffusion of materials, it is essential to conduct ALD at low temperatures while adhering to a limited thermal budget.[102] In this thesis, a PICOSUN® R-200 Standard ALD system was used for deposition. The deposition was conducted at 120 C with N$_2$ gas as the precursor carrier gas. It is important to emphasize that this reactor is not a fluidized bed reactor. The fluidization, in a fluidized bed reactor ALD (FB-ALD), is a technique for suspending the substrate particles, thus ensuring near maximal exposure of surface area for coating. In the reactor used for this particular work, however, the powder is stationary during the coating procedure. This means that there is a high possibility that

a complete coverage of the particles surface cannot be reached. The ALD deposition cycles used in this work can be described as follows:

Recipe 1. (**Paper I–III**) (i) TMA/TiCl$_4$ was pulsed for 0.2 sec at a flow rate of 15 sccm into the ALD reactor chamber (where the powder substrate is situated), followed by a purge with the carrier gas, at a flow rate of 100 sccm. This step was repeated 10 times to achieve a net pulsing time of 2 sec. (ii) the reactor was purged with carrier gas for 60 sec at flow rate of 600 sccm. (iii) H$_2$O was pulsed for 0.2 sec at a flow rate of 15 sccm followed by purging with carrier gas at a flow rate of 100 sccm. This step was repeated 10 times to achieve a net water pulsing time of 2 sec. (iv) the reactor was purged by carrier gas for 60 sec at a flow rate of 600 sccm. The described steps complete one ALD deposition cycle (Figure 2.1).

Recipe 2. (**Paper IV**) Same as *recipe 1*. However, the pulse time for TMA and H$_2$O precursors was increased to 0.5 sec, where a net precursor pulsing time of 5 sec was achieved. Additionally, the coating cycles were terminated with a pulse step of H$_2$O precursor.

2.2 Fluorine selective probe

The concept of pH is technically limited to aqueous solutions and determining pH in organic electrolytes is challenging. Although proton activity is as applicable to organic mediums as in aqueous, the organic solvents which are proton deficient compared to water give unstable pH readings. The insulating character of organic solvents also makes most pH measurement methods inapplicable because they are based on electric current or charge transfer through the solution. An explicit approach to characterize acidity in our system is to determine the concentration of the acid in question (HF), which is proven to be prevalent in LiPF$_6$ containing electrolytes. The determination of HF in this thesis was therefore performed with a F$^-$ sensitive ion selective electrode (ISE, Mettler Toledo perfectION combination fluoride electrode). The technique is implemented based on a method developed for F$^-$ determination in LiPF$_6$ electrolytes presented by Strmcnik *et al.*[106] The F$^-$ ISE was calibrated with a series of standards containing a known amount F$^-$ ions, prior to measurements. The calibration standards were water based with NaF as a fluorine source. Calibration standards containing F$^-$ concentration ranging from 0.5 ppm – 500 ppm were used to formulate a calibration curve, which was subsequently used to determine HF in the electrolytes (Figure 2.2a). A 50:50 vol. % of water and total ion strength adjustment buffer (TISAB) with (1,2-Cyclohexylenedinitrilo)tetraacetic acid (CDTA) was used as a base, to compensate for charge contributions from impurities. The sampled organic electrolyte was thus transferred in to the base

solution. The potential of the fluoride electrode (with an internal reference electrode) or the potential of the fluoride electrode with relation to a reference electrode immersed in H_2O:TISAB mixture was then recorded. The concentration could thus be determined from the calibration curve. Counterintuitively, the dilution of the non-aqueous electrolytes containing $LiPF_6$ in TISAB effectively halts any further hydrolysis of $LiPF_6$, hence enabling this type of study. For comparison, a similar calibration curve is provided for Tetrahydrofuran/ Tetra-n-butylammonium fluoride (THF/TBAF) in DEC solution, which coincides well with the water:TISAB calibration curve (Figure 2.2a). However, aqueous based measurements were chosen in **Papers IV–VI** for the sake of simplicity.
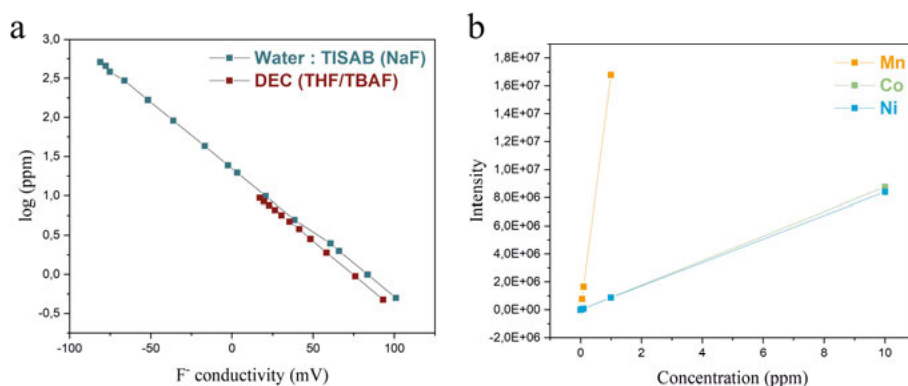

Figure 2.2. (a) Calibration of the fluoride ion selective electrode (ISE) with aqueous solution (NaF in water:TISAB) and non-aqueous solution (THF/TBAF in DEC). (b) ICP-OES calibration with different standard concentrations of Co, Mn, and Ni provided from Multi-element Calibration Standard.

2.3 Inductively coupled plasma atomic emission spectroscopy

ICP-OES is a technique used in this thesis to determine the quantity of different elements. In general, these elements have detection limits in the µg/l (ppb) range. During measurement, liquid samples are nebulized into an aerosol, which is a fine mist of the sample droplets injected. The aerosol is subsequently carried to a plasma core by carrier gas (typically Ar). RF (radio-frequency) current oscillation, typically 27 to 40 MHz, creates RF (radio-frequency) electric and magnetic fields in copper coils. A flame is added to the gas as Ar gas swirls around the torch, enabling the separation of certain electrons from argon atoms. These electrons are those that the magnetic field captures and excites. Applying energy to electrons in this manner is referred to as "inductive coupling." In exchange, these high-energy electrons collide with other argon atoms, which results in the loss of more electrons. In a chain reaction, collisional ionization of

the argon gas continues, decomposing the gas into a plasma made of argon atmosphere, electrons, and argon ions, resulting in what is known as an inductively coupled plasma discharge. Until the sample aerosol is dissolved, vaporized and atomized, the plasma serves two functions: ionization and excitation of the introduced sample. Emission is achieved when the level of an atom or ion reaches an excitation phase. Since the best emission lines of many elements are formed by excited ions from the ICP, certain elements will also need to undergo ionization. Every element has a distinct set of energy levels and, consequently, a distinct set of absorption and emission wavelengths. The excited atoms and ions emit their characteristic radiation, which is then distinguished with a mono- or polychromator before being detected and converted into electrical signals, which are then converted into concentration. Calibration is performed prior to analysing samples so that concentrations of elements of interest can be calculated. This is done by creating a calibration curve (function) for standard solutions that contain a known concentration of the element of interest.

The main analytical advantage of the ICP over other emission sources is derived from the ability of ICP to vaporize, atomize, excite and ionize efficiently and reproducibly quantify a wide range of elements in many different sample types. The distribution of concentrations from the lower measurement limit to the upper limit is known as the emission line's linear dynamic range (LDR). Exceeding these limits results in high standard deviation (STD) or saturation, respectively. For ICP-OES, the upper limit of linear calibration is normally 104 to 106 times the limit of detection for a given emission line. For example, for the Mn 257.610 eV emission line, the highest linear concentration is about 50 mg/L, or about 105 times its detection limit of 0.0004 mg/L. For accuracy and reproducibility, all ICP measurements presented in the thesis have < 5 % STD.

2.4 Other characterisation methods

Electrochemical characterization. Galvanostatic cycling (chronopotentiometry) was *explicitly* used for electrochemical characterization. Here, a constant current is applied between the working and counter electrodes to drive electrochemical reactions (and a reverse current to drive the reverse reactions) in a specified voltage window. This provides useful information with regards to cell capacity, the average potential and long-term cyclability. In addition, Coulombic efficiency (CE) as a ratio of discharge capacity over charge capacity can be calculated to describe the reversibility of electrochemical reactions. The flow of Li^+ or electrons should be fully reversible from the electrochemical reactions, assuming no side reactions in the electrodes in an ideal cell; CE would then be equal to 100%. However, in reality there are pervasive side reactions between electrolytes and electrodes. This contributes to the CE value deviating from 100%, which offers information on the presence of side/parasitic reactions. Potentiometric intermittent titration technique (PITT) has also been used

in **Paper V**, where potentiostatic charge pulses are applied, each followed by a period of relaxation, until the potential limit is reached. In *lieu* of linear sweep voltammetry (LSV), this technique was used to determine the oxidative stability of electrolytes.

Coulometric Karl Fischer. As stated in **section 1.4**, the presence of water plays a crucial, albeit indirect, role in the dissolution of TMs. In this study, a Karl Fischer (KF) coulometric measurement was used to determine the water concentration in electrolytes. In the titration cell, a KF-specific reagent is combined with a solvent. An electrical current trigger the release of reagent when a sample is dissolved in the titration cell containing KF-specific reagent and solvent. The amount of current required to convert water into reagent determines the amount of moisture.

Scanning electron microscopy and Transmission electron microscopy. Confirmation of conformality and homogeneity of the ALD deposited thin film is necessary, and thus a high spatial resolution imaging is required, which scanning electron microscopy (SEM) and transmission electron microscopy (TEM) can offer. Thus, SEM and TEM were utilized in **Papers I–IV**.

X-ray Photoelectron Spectroscopy. In x-ray photoelectron spectroscopy (XPS), x-ray radiation is directed at a sample in an ultra-high vacuum chamber, and the kinetic energy of the photoelectrons released from the sample by the photoelectric effect is determined by an electrostatic analyser. This technique characterizes the surface chemical composition of the sample to a depth of a few nanometres, making it ideal for the ALD-deposited thin film. In order to confirm the presence of ALD thin films on coated substrates, this method was utilized as a complementary technique. Additionally, the chemical composition of cycled electrodes was also analysed by XPS in **Papers I–V**.

Brunauer–Emmett–Teller (BET). Electrode reactions, whether chemical or electrochemical, depend on the surface area of reactants. Therefore, it is necessary to determine the surface area of the investigated active materials. The ALD coating thickness was estimated in **Papers I–IV** using the BET surface area in conjunction with ICP quantification of the coating elements present.

3 Scope of the thesis

This thesis explores ageing mechanisms of cathode materials, with an emphasis on TM dissolution and on strategies to mitigate the ageing from two perspectives. Based on **Papers I–IV**, the first part considers the strategy of modifying the cathode surface. As discussed in **section 1.5**, the structural integrity of high voltage cathodes in a delithiated state is a challenge that must be addressed since Ni-based layered TM-oxides have been shown to undergo phase transition to spinel and then to rock-salt structures, accompanied with a release of lattice oxygen.[26,48] Similarly, spinel TM-oxide surfaces transform into rock-salt structures.[49] The formation of an electrochemically inert rock-salt structure due to surface reconstruction substantially increases cathode impedance.[51] Several investigations have also demonstrated that the onset potential for oxygen release correlates well with the onset of CO and CO_2 evolution triggered by irreversible electrolyte degradation.[53] This leads to the second strategy of mitigating the cathode ageing; avoiding chemical and electrochemical degradation of organic electrolyte solutions at high potentials. The limited anodic stability of standard carbonate-based electrolytes at E ~4.5 V *vs.* Li/Li^+ makes high-voltage cathode performance very problematic; hence, electrolyte modification is investigated in the second part of the thesis, based on **Papers I** and **IV–VI**.[107]

From the cathode surface perspective, atomic layer deposition (ALD) coating of a variety of cathode materials with Al_2O_3 and TiO_2 coatings is investigated as a method to stabilize the cathode/electrolyte interface and to minimize TM dissolution. From the electrolyte perspective, the role of salt (a comparative study of $LiPF_6$, LiBOB and $LiClO_4$), solvent (a comparative study of SL and EC), and additive (LiDFP) on TM dissolution are here investigated. Furthermore, the chemical and electrochemical dependence of TM dissolution mechanism are discussed within the two perspectives.

4 Results and discussion

4.1 Cathode surface modification

4.1.1 Characterization of ALD oxide coatings

As discussed in **section 2.1**, during ALD deposition, atoms and molecules are incident on a substrate (cathode), where they chemically react and form a thin film. Thus, deposition parameters such as deposition temperature and the composition of the substrate influence the formation of the film. If the energy available to the depositing species, *i.e.* temperature is low, an amorphous and/or porous structure would form since the sluggish mobility molecules or atoms sluggish mobility prevents them from moving to the optimal positions.[108] Due to the low deposition temperature (120 °C) used in this thesis, insignificant change (negligible cation diffusion) is expected in the bulk LNMO (see XRD diffractograms in Figure 1 in **Paper II** and **III**). In order to manipulate the crystallinity of the coating layer and increase the interfacial bonding between the cathode substrate and the coating layer, higher deposition temperatures and/or post-deposition heating procedures can be used.[109] However, interdiffusion of the coating material into the bulk is a potential additional consequence that requires careful parameter optimization, which was not investigated in this thesis. Based on the Raman spectra of the coated LNMO materials, it can further be established that the coating method had no discernible effect on the bulk LNMO (Figure 1 in **Paper II** and **III**). XPS analysis of LNMO and LMO powders coated with Al_2O_3 and LNMO coated with TiO_2 confirmed the presence of Al and Ti on the cathode surfaces, respectively. Figure 4.1(f) depicts an example of XPS spectra comparing pristine and coated samples; for further information, see **Papers I–III**. Figure 4.1(a and g) depict the cross-section of LNMO powder coated with Al_2O_3 and TiO_2 with 20 ALD cycles, denoted as "20 ALD Al_2O_3" and "20 ALD TiO_2", obtained by STEM coupled with electron energy loss spectroscopy (EELS). The annular dark-field (ADF)-STEM micrographs also show the uniformity and thickness of the coating layers. On the surface of crystalline LNMO, an amorphous layer with a uniform thickness of roughly 2 nm Al_2O_3 is observed. Similarly, TiO_2 has a thickness of 1 nm on the TiO_2 coated LNMO. The coatings cover all the inner and corners of facets.

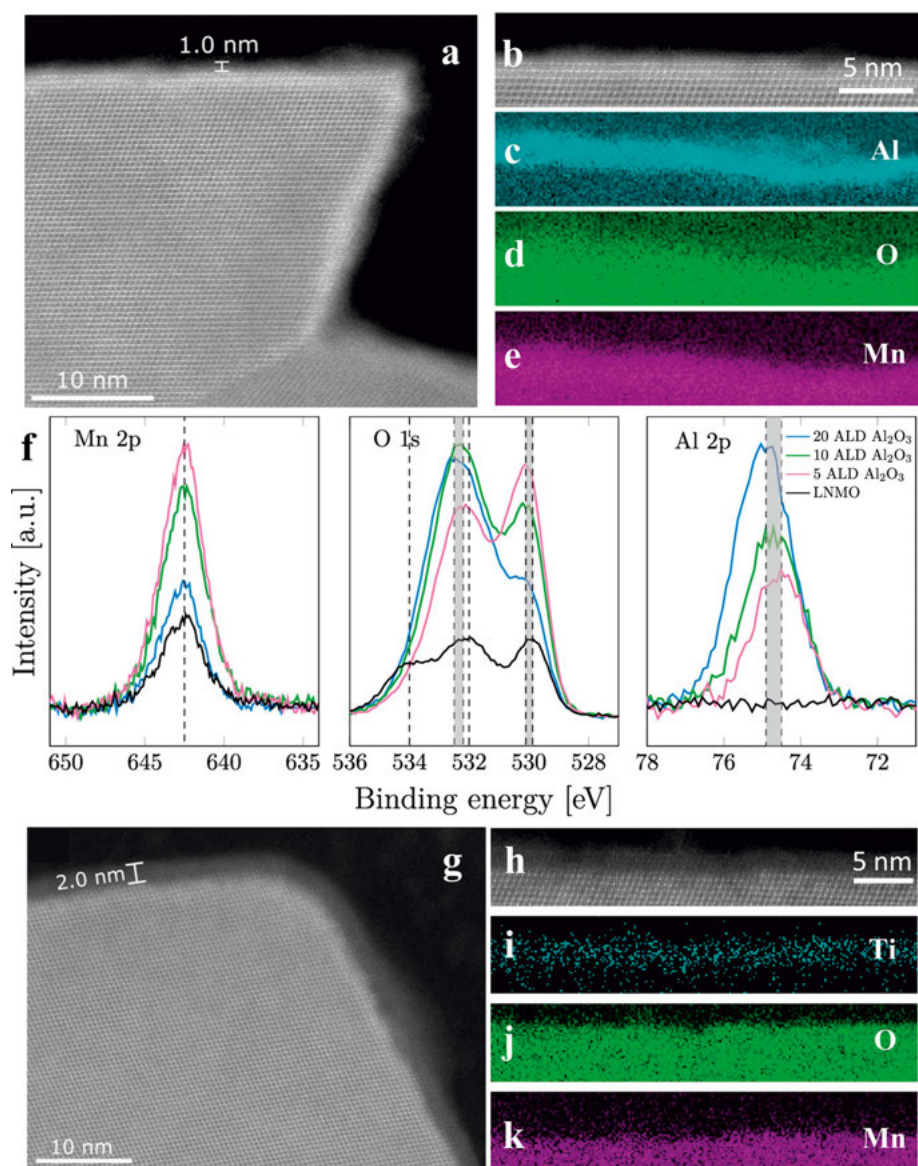Figure 4.1. STEM results from the cross section of a 20 ALD Al_2O_3 particle. (a) ADF-STEM micrograph showing the uniformly thick coating over a facet corner. (b) Higher magnification ADF-STEM image of coating on a facet. (c−e) Corresponding EELS elemental maps from the Al−K, O−K, and Mn-$L_{2,3}$ core loss edges, showing the presence of aluminum oxide. (f) Mn 2p, O 1s, and Al 2p XPS spectra for the pristine LNMO (black), 5 ALD Al_2O_3 (pink), 10 ALD Al_2O_3 (green), and 20 ALD Al_2O_3 (blue). STEM results from the cross-section of a 20 ALD TiO_2 particle before cycling. (g) Annular dark-field (ADF)-STEM micrograph showing the uniform coating with a thickness of less than 1 nm. (h) ADF-STEM image with atomic resolution showing the TiO_2-coating on a facet. (i–k) Corresponding EELS elemental maps from the Ti-K, O-K, and Mn-$L_{2,3}$ core loss.

Although TEM is a highly accurate technique, the few particles examined here are not necessarily representative of all coated particles. Thus, total coverage of the surface area of the particles is not guaranteed. Refer to **section 2.1** for more information on the type of ALD system utilized in this thesis. This makes characterizing the actual uniformity of the coatings challenging. Furthermore, the density of amorphous materials, such as Al_2O_3 and TiO_2 films produced at low temperatures, can vary with film growth/deposition temperature. Additional independent thickness measurements are required to evaluate the density from *e.g.*, quartz crystal microbalance (QCM) mass measurements, however this is not covered in the thesis.[110]

According to Groner *et al.*, the density of low temperature ALD coated Al_2O_3 films ranges from 2.5 g/cm³ at 33 °C to 3.5 g/cm³ at 177 °C.[110] Similarly, Piercy *et al.* showed that the density of low-temperature ALD-coated TiO_2 films is 3.25 g/cm³ to 3.68 g/cm³ when temperature is ranged between 38 C and 125 °C.[111] While ALD has been shown to provide excellent and consistent coatings on flat surfaces, it is difficult to maintain conformity when coating porous and powdered materials.[112] Therefore, research on ALD coated cathodes generally, and correctly, relies on TEM images for qualitative assessment. The coating thickness can be <u>estimated</u> using Al or Ti quantified in the powders by ICP and the estimated density of the respective Al_2O_3 and TiO_2 structures, as described in **Papers I–IV**. The estimated thicknesses presented in this thesis, however, should be taken with consideration and should only be utilized when comparing a coating growth in a specific sample. Thus, the thickness estimation should not be used to compare two distinct cathode materials with diverse properties, such as surface area, particle size distribution, and structure. The estimated thicknesses **Papers I–IV**, however, give a sufficient correlation with reported film growth rates of ~1.1 – 1.3 Å/cycle of Al_2O_3 and ~0.6 Å/cycle of TiO_2.[100,105]

4.1.2 Beneficial role and limitations of ALD oxide coatings

As noted in **section 2.1**, most studies on the impact of Al_2O_3 coating on cathode surface have shown positive response in improving electrochemical performance. However, there are conflicting views on how Al_2O_3 contributes to the favourable effects observed on electrochemical cycling. Similar experiences are discussed in this subsection.

<u>Figures 4.2(c and e)</u> show long term half-cell cycling of pristine and 5 cycle Al_2O_3 coated LCO and NMC coated with *recipe 1* (see **section 2.1** for information on recipe). When the cathodes are ALD coated with Al_2O_3, there is a noticeable increase in capacity retention. <u>Figure 4.3</u> depicts LMO‖LFP cells coated with two different thicknesses of Al_2O_3, termed "5CALD" and "10CALD". The thickness of the coating corresponds to a 5 and 10 cycle ALD deposition with *recipe 1*. Here, the coating is less effective, since there is no discernible difference between the PLMO (uncoated) and 5CLMO in terms of

capacity retention. The 10CLMO sample, on the other hand, shows a lower initial capacity and a larger overpotential. <u>Figure 4.4</u> (from **Paper II**) shows a similar pattern for LNMO coated with Al_2O_3. 10 and 20 cycle coated LNMO electrodes exhibit lower capacity and higher overpotentials than uncoated LNMO electrodes. The capacity retention of the 5-cycle coated LNMO electrodes, however, shows minor improvement at 25 °C.
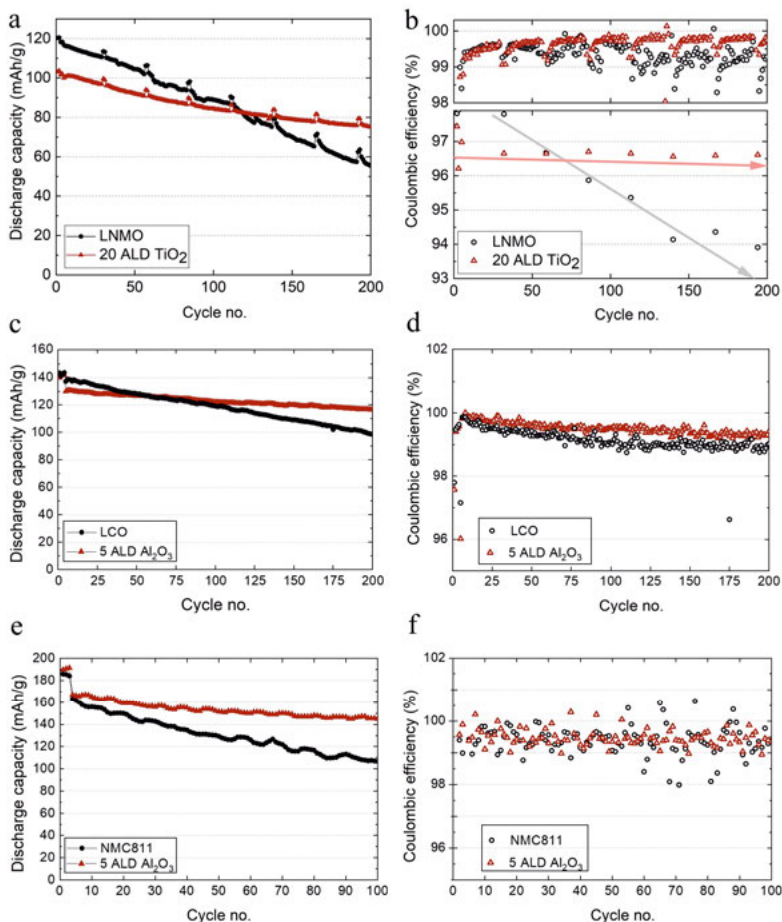

Figure 4.2. (a) Discharge capacity and (b) Coulombic efficiency per cycle for LNMO (black) and 20 ALD TiO2 (red) full-cells with graphite counter electrode. The lower Coulombic efficiency values upon change in C-rate are shown in the lower part of (b) with trends for LNMO and 20 ALD TiO_2 indicated by arrows (gray and pink, respectively). After the four formation cycles of C/10 and C/4, the cells are cycled at C/2 with two C/10 cycles every 25th cycle. (c) Discharge capacity and (d) Coulombic efficiency per cycle for LCO (black) and 5 ALD Al_2O_3 (red) half-cells with graphite counter electrode. (e) Discharge capacity and (f) Coulombic efficiency per cycle for NMC (black) and 5 ALD Al_2O_3 (red) half-cells with graphite counter electrode.
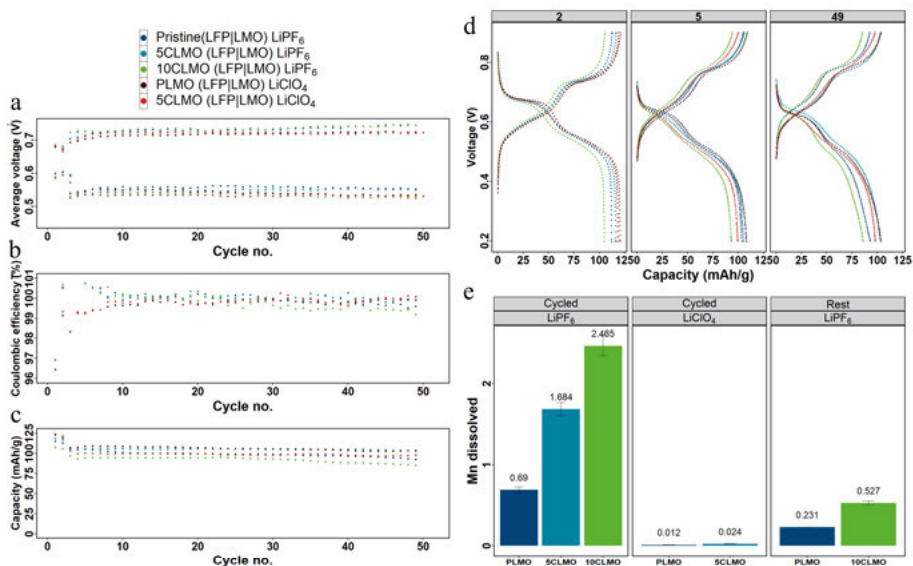
Figure 4.3. Galvanostatic cycling of LFP∥LMO cells with $LiPF_6$:EC:DEC and $LiClO_4$:EC:DEC electrolytes and relative Mn dissolution determination by ICP-OES. First two cycles were performed at C/5 and 47 at 1C, between 0.2 and 0.9 V (corresponding to between 3.5 and 4.3 V vs. Li/Li^+). (a) average voltage. (b) capacity retention. (c) Coulombic efficiency. (d) 2nd cycle at C/5 and 5th and last cycle at 1C. (e) %Mn dissolution into the electrolyte from the cycled and rested LMO electrodes in LFP∥LMO cells. The rested cells where left at OCV for the same amount of time as the cycled cells.

There are mixed reports that suggest an increase in overpotential following ALD coating of cathodes with Al_2O_3, as well as studies that support a decrease in overpotential. Similarly, initial capacity has been shown to increase or decrease following ALD coating. The amorphous, electrically insulating Al_2O_3 with a band gap of 6.9 eV should naturally increase overpotential, if the cathode particles are completely covered.[113] Furthermore, the Li^+ diffusion barrier in Al_2O_3 structure is inherently larger than in conventional TM-oxide cathode materials.[114] As the thickness of the coating increases, the aforementioned characteristics will inevitably be amplified.

Kang *et al.* demonstrated that electrochemical rate capability, capacity retention, and interfacial impedance depend on more than just the near-surface oxidation states of TMs. It is also affected by the Al_2O_3 coverage of the cathode particles.[115] Non-uniform coating results in non-uniform Li^+ conduction routes, where Li^+ primarily flow in and out of the particle at select and electrochemically active sites where the coating is thinner or absent. The effect is exacerbated by thicker Al_2O_3 coatings, as non-uniformity will likely increase. This creates a non-uniform ageing of the cathode surface, making these active sites more vulnerable to attack by acidic species or leaching agents in the electrolyte (*e.g.*, HF). Figure 4.4 shows an example of this phenomenon when LNMO is

20 cycle ALD coated with Al_2O_3 (*recipe 1*) and is cycled in a half-cell setup at 50 °C. The surface of the primary particles of the electrode has visible holes. The holes have a rather large diameter (up to 100 nm) and extend into the active material. None of the compared electrodes (pristine, 5 cycle ALD coated, or 10 cycle ALD coated) cycled at 50 °C showed any LNMO particles with visible holes that could be observed with SEM. It, however, does not exclude the possibility of smaller pinholes that are not apparent. This is further reflected with Figure 4.3, where Al_2O_3-coated LMO demonstrated increased Mn dissolution in LFP‖LMO cells when compared to uncoated LMO.
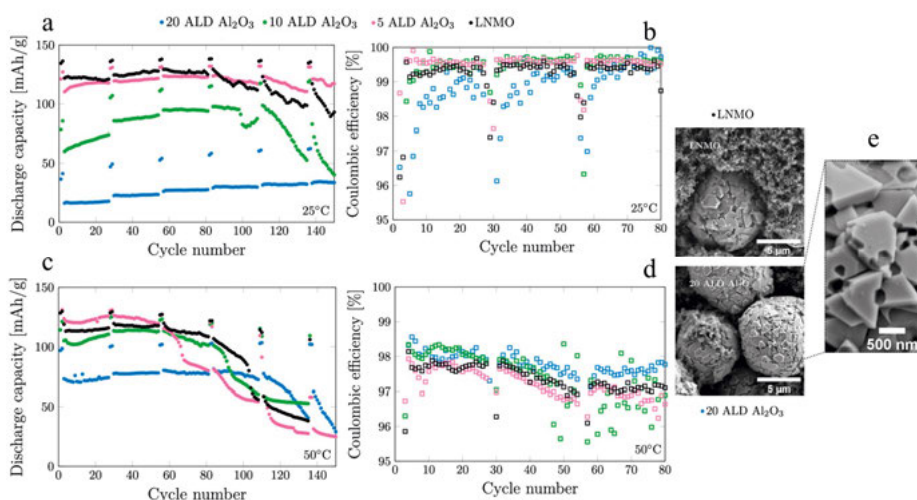

Figure 4.4. Discharge capacity and Coulombic efficiency for the cells cycled at room temperature (a,b) and the cells cycled at 50 °C (c,d) for pristine LNMO (black), 5 ALD Al_2O_3 (pink), 10 ALD Al_2O_3 (green), and 20 ALD Al_2O_3 (blue). The C-rates are C/2 for all cycles with two C/10 cycled every 25 cycles. Due to the large variation in cell behavior at 50 °C, the discharge capacity in (c) is the average value from 3 to 5 cells. The slow charging cycles (C/10) every 25th cycle is added to gain information about the origin of the capacity fade. (e) SEM micrographs showing LNMO (top) and 20 ALD Al_2O_3 (bottom) electrodes cycled at 50 °C for 270 cycles.

In contrast, Figure 4.2(a and b) depicts the cycling performance of LNMO‖graphite cells containing pristine or TiO_2 coated LNMO, designated as "pristine" and "20 cycle LNMO", respectively. The coating conditions and procedure was identical for TiO_2 coating shown in Figure 4.2a and for Al_2O_3 presented in Figure 4.4a. Despite having a lower initial capacity, the 20 cycle TiO_2 coated LNMO demonstrates a significant increase in capacity retention. The TiO_2 coated LNMO did not exhibit the same pinhole evolution as Al_2O_3 at elevated temperature (see **Paper II**). The TiO_2 coating, which has a bandgap of 3.2 eV – 3.4 eV and a higher ionic conductivity than Al_2O_3, is considered to provide a more uniform Li^+ conduction while simultaneously functioning as a

protective layer. Post-mortem XPS analysis of the TiO_2 and Al_2O_3 coated LNMO electrodes revealed that the electrode surface was fluorinated. This is consistent with prior studies on the formation of TiF_4 and AlF_3 in the presence of a fluorinated salt in the electrolyte. This clearly shows the reactivity of the coating to the acidic environment that the electrolyte provides, such as serving as an HF scavenger. The amount to which electrolyte acidity or HF is produced will be addressed in the following sections. For both pristine and coated LNMO samples, XPS analysis of the counter electrodes revealed the presence of Ni and Mn. This suggests neither TiO_2 nor Al_2O_3 prevented TM dissolution completely. However, at the 4.7 V the average working potential of LNMO, several electrolyte components are unstable and undergo degradation processes releasing various species that are corrosive towards the cathode surface, as discussed in **section 1.4**.

Figure 4.2 and the studies in **Papers I**–**III** demonstrate both the benefits and limits of amorphous Al_2O_3 as a coating material *during* electrochemical cycling. Despite the abundance of information reported for Al_2O_3 in terms of enhancing capacity retention by functioning as a protective layer, there is still much to learn about the electrode-coating interfacial structure-property relationships that contribute to electrochemical performance. The presented mixed trends for Al_2O_3 coated on diverse cathodes, in this thesis, emphasizes the significance of tailoring the coating technique based on the substrate/cathode, film precursors, and resultant coating material. Oxide coatings should, in general, be (i) ultrathin (sub-nm), (ii) uniform with complete particle coverage, and (iii) conformal. Substrate or cathode characteristics such as (i) surface area (ii) particle size distribution (iii) cathode crystal structure and the associated TMs in the structure should be considered to achieve this. It is also critical to guarantee that the full surface area of cathode particles is exposed to ALD precursors during the coating procedure.

When not subjected to electrochemical cycling, *i.e.* no Li^+ transport into or out of particles, the presence of a protective oxide layer, even if it does not provide total cathode particle coverage, should have a positive effect on the cathode against the harsh environment often provided by conventional electrolytes. This is investigated further in **Paper IV** by delving into the chemical ageing of cathode materials and the interplay with Al_2O_3 coating (discussed in **subsection 4.2.2)**.
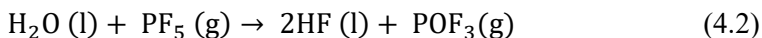
4.2 Electrolyte modification

Based on **Papers I** and **IV–VI**, this section discusses the chemical and electro-chemical TM dissolution profiles of various cathode materials and the interplay with the previously described Al_2O_3 coating material. The section also discusses the impacts of electrolyte components on TM dissolution.

4.2.1 Role of electrolyte salt ($LiPF_6$) on TM dissolution

Papers I and **V** addressed a comparative evaluation of $LiPF_6$ conducting salt in TM dissolution process. **Paper I** demonstrated an increase in Mn dissolution from LMO with $LiPF_6$-based electrolytes as compared to $LiClO_4$-based ones. The amount of dissolved Mn-ions in the electrolyte was two orders of magnitude greater in LFP‖LMO cells containing $LiPF_6$ than in similar cells containing $LiClO_4$ (Figure 4.3). The most often reported $LiPF_6$ hydrolysis pathway is based on a multi-step process involving salt dissociation that produces lithium fluoride (LiF) as a solid and phosphorus pentafluoride (PF_5) as a gaseous product (reaction 4.1). Traces of H_2O in the electrolyte may then participate in re-action with PF_5, resulting in the formation of hydrogen fluoride (HF) and phosphoryl fluoride (POF_3), (reaction 4.2).[69,73,116–118] Thus, HF has the potential to engage in subsequent TM-oxide corrosion.

$$LiPF_6(s) \rightleftarrows LiF\ (s) +\ PF_5(g) \qquad\qquad (4.1)$$

$$H_2O\ (l) +\ PF_5\ (g) \rightarrow\ 2HF\ (l) +\ POF_3(g) \qquad\qquad (4.2)$$

To eliminate the influence of HF on TM dissolution, Gallus *et al.* investigated replacing $LiPF_6$ with the less hydrolysis sensitive $LiBF_4$ and the fluorine-free conducting salt $LiClO_4$.[119] $LiPF_6$ was determined to be the most detrimental salt, with $LiClO_4$ displaying minimal dissolution and $LiBF_4$ effectively mitigating dissolution. Previous research has also shown that the oxidation of the perchlorate anion generates a perchlorate radical as a primary product (reaction 4.3), which can then react with other organic electrolyte components (R–H), mostly generating perchloric acid (reaction 4.4).[120]

$$CLO_4^- \rightarrow\ CLO_4^\bullet +\ e^- \qquad\qquad (4.3)$$

$$CLO_4^\bullet + R\text{--}H \rightarrow\ HCLO_4\ + R^\bullet \qquad\qquad (4.4)$$
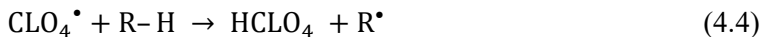
This process, however, is electrochemically prompted and has been found to be prevalent at $E > 4.4$ V vs. Li/Li^+.[121] These by-products have the capacity to have a parasitic effect on the cathode surface, which can explain the observed dissolution in the $LiClO_4$-containing electrolyte (Figure 4.3). In line with Paper III, Paper V compared $LiPF_6$-based and LiBOB-based electrolytes which had been

cycled in LMO||LFP and NCA||LFP cells. The presence of a fluorinated salt significantly contributes to TM dissolution, whereas LiBOB does not. Thus, the following hierarchy is established for the investigated conducting salts in terms of TM dissolution, with LiBOB demonstrating the lowest: $LiPF_6$ > $LiClO_4$ > LiBOB. In addition to reactions 4.1 and 4.2, several autocatalytic mechanisms are involved in the generation of HF during electrochemical cycling will be addressed in the following sections. Nonetheless, Papers I and V show that the presence of $LiPF_6$, and hence HF, in the electrolyte solution is a primary cause of TM dissolution, and thus regulating electrolyte acidity is critical.

Furthermore, non-cycled LMO||LFP cells show a significant amount of Mn-ion dissolution relative to cycled cells as illustrated in Figure 4.3 ("Rest", *i.e.* no current/potential is applied). This indicates that both chemical and electro-chemical-activated processes cause TM dissolution. Considering this observation from **Paper I**, the next section (detailed in **Paper IV)** explores the chemical TM dissolution process of lithiated and delithiated LMO and NMC in a typical Li-ion electrolyte which had already been exposed to hydrolysis and HF formation.

4.2.2 Emphasis on chemical TM dissolution

Mn dissolution has received the most attention thus far, as it is thought to explain the predominant failure mechanism in spinel LMO. As described in **section 1.4**, LMO contains equal Mn^{3+} and Mn^{4+} ratios. Hunter C. [122] proposed the commonly accepted explanation for Mn dissolution as a disproportionation reaction of Mn^{3+}, yielding Mn^{2+} and Mn^{4+}. The Mn^{2+} species are proposed to have increased solubility in the electrolyte, as described in **section 1.6**. However, Mn dissolution has also been reported to accelerate at higher states of charge (SOC), where the Mn^{4+} oxidation state dominates, contradicting a dissolution process primarily initiated by disproportionation.[34–37] Mn dissolution has also been observed in mixed TM layered oxides (NMC), which contain only structural Mn^{4+}, indicating that the disproportionation process is unlikely.[60,81] **Paper IV**, thus, investigates the TM dissolution process of lithiated and delithiated LMO and NMC811 powder in $EC:DEC:LiPF_6$ (LP40) electrolyte. Furthermore, the LMO and NMC were ALD coated with Al_2O_3 using *recipe 2* to determine the coating's role in the chemical TM dissolution process (see SEM images in Figure 1 of **Paper IV**). To initiate and propagate $LiPF_6$ hydrolysis, 2000 ppm of H_2O was added to the LP40 electrolyte's stock solution. After 14 days of storage, the electrolyte formed 4300 ppm HF, which is slightly more than the predicted 4000 ppm HF according to reaction 4.1 and 4.2. Clearly, the presence of H_2O affects not only the salt but also the solvents (*e.g.*, EC is susceptible to hydrolysis), resulting in additional HF.[123]

The LMO and NMC811 powders were subjected to a NO_2BF_4 oxidant dissolved in the highly anodically stable solvent acetonitrile for delithiation (see

experimental section of **Paper IV**). The residual lithium content was determined by ICP-OES to be 70 % for delithiated PNMC and 47 % for 10CNMC. Similarly, the composition of delithiated PLMO and 10CLMO was determined to be $Li_{0.45}Mn_2O_4$ and $Li_{0.32}Mn_2O_4$, respectively. "P" and "10C" in the sample nomenclature refer to pristine and 10 cycle Al_2O_3-coated active materials, respectively. Thus, the ALD coated active materials were found to be 30 % and 13 % more delithiated than the pristine NMC and LMO, respectively. It is likely that coating increases the mechanical integrity of the active materials, resulting in reduced crack development during delithiation and thus promoting a more homogeneous delithiation. Higher surface area particles have correspondingly higher interaction with NO_2BF_4 and hence a higher delithiation degree. Since LMO has ×6 higher surface area than NMC (see Table 1 in **Paper IV**), this can explain the observed discrepancies.
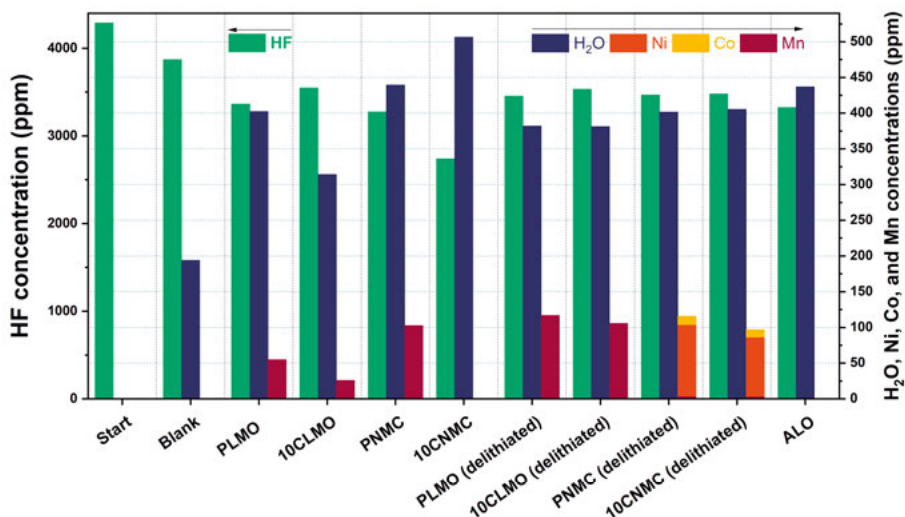

Figure 4.5. Measured HF, H_2O and TM concentrations of lithiated and delithiated state NMC and LMO, as well as Al_2O_3 as a reference, after exposure to an aged electrolyte for 24 hrs. Adding 2000 ppm H_2O to a stock LP40 electrolyte led to the formation of 4300 ppm HF after 14 days of storage ("Start"). A "Blank" sample is included, in which the "Start" solution was transferred to a fresh vial without any contact with active materials for the duration of the soaking experiment (24 hrs).

Figure 4.5 shows the measured HF, H_2O and TM concentrations of lithiated and delithiated NMC and LMO, as well as Al_2O_3 as a reference, after exposure to an aged electrolyte for 24 hrs. When the aged electrolyte encounters the active materials for 24 hrs, there is a significant decrease in HF and an increase in H_2O content. A substantial portion of the HF consumed and H_2O generated can be explained by an acid-base reaction in which the powders neutralize the acidity of the electrolyte.

The alkalinity of the powders was evaluated by soaking the powders in Milli-Q H_2O (deionized water with a resistivity > 18.2 MΩ cm) and monitoring the pH change, from which the number of released OH$^-$ per powder surface area was calculated (Figure 4.5). The following alkalinity hierarchy is formed for the active materials, with amphoteric Al_2O_3 displaying the lowest: NMC > LMO > Al_2O_3. Since NMC has one more Li per TMO_2 unit than LMO, it is expected to be more alkaline. Delithiated LMO and NMC powders have lower OH$^-$ release than lithiated equivalents, and hence are predicted to be less alkaline. Figure 4.5 further demonstrates that, although the Al_2O_3 coating decreases the respective powder alkalinity, both the coated LMO and NMC active materials retain a significant capacity to neutralize an acid. This may be due to the presence of uncoated regions on the surface of the active materials. This also supports the possible nonuniformity of the Al_2O_3 coating discussed in **section 4.1**.
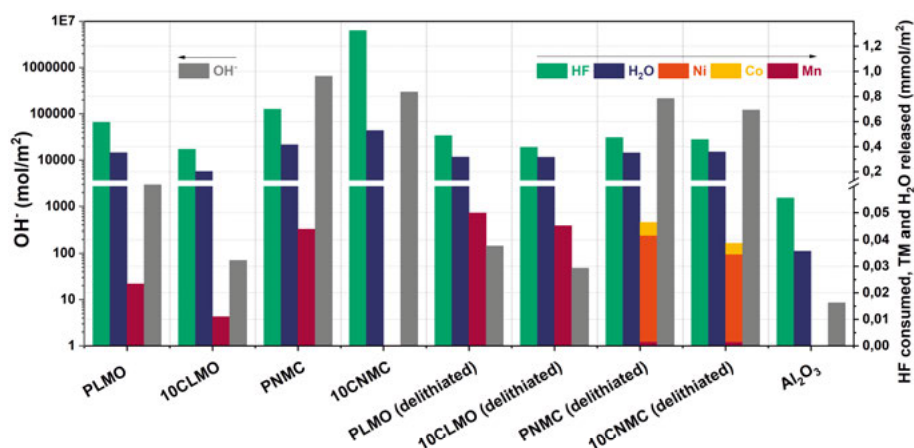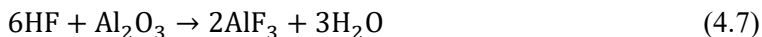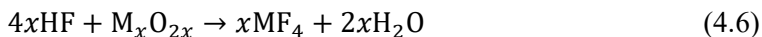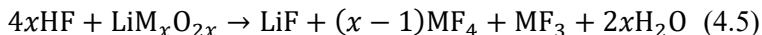

Figure 4.6. HF consumption, TM dissolution and H_2O formed from soaking experiments of pristine and Al_2O_3 coated LMO and NMC as well as Al_2O_3 powder, standardized by surface area. Alkalinity of powders estimated by the OH- released according to surface area when soaked in aqueous 0.001M KCl.

Taking cognizance of the above stated acid-base interaction, a residual percentage of HF is expected to be involved in active material dissolution. The concentration of TMs in the aged electrolyte increased to around 50 ppm – 100 ppm for pristine LMO and NMC. Despite having a lower alkalinity, or proclivity to neutralize the HF, the Al_2O_3 coating significantly reduced the degree of TM dissolution from the active materials. Still, a decrease in HF concentration and an increase in H_2O concentration is observed for pure Al_2O_3 powder in contact with the aged electrolyte. The quantity of HF consumed, H_2O and TMs released normalized by surface area of the powders are displayed in Figure 4.6, to compare the reactivity of the powders. The soaking experiment was specifically designed to expose the same amount of HF to the same surface area of the

powders. Thus, ×6 more NMC powder was soaked in the same volume of aged electrolyte as in LMO, due to the ×6 larger surface area of the latter. Except for the highly alkaline lithiated NMC powders, all active materials consumed around the same moles of HF (0.5 ± 0.1 mmol/m^2) and generated approximately the same moles of H_2O (0.3 ± 0.1 mmol/m^2). Al_2O_3 also shows a comparable ~2HF/H_2O ratio, but the reaction proceeds to a smaller extent due to its lower alkalinity. The higher the driving force for HF to react, the higher the alkalinity of the powders. This is demonstrated by the consumption of more HF/cm^2 by the lithiated NMC. Based on the observed ~2HF/H_2O ratio, **Paper IV** proposes reactions 4.5 and 4.6 for lithiated and delithiated active materials, respectively. M is Ni, Co, or Mn and x is either 1 or 2 depending on whether we consider layered NMC or spinel LMO. We also proposed reaction 4.7 for Al_2O_3. The molar ratios of HF consumed to TM dissolved ranged from $4 - 10$, illustrating the significance of the investigated acid-base reaction in determining TM dissolution from cathode active materials.

$$4x\mathrm{HF} + \mathrm{LiM}_x\mathrm{O}_{2x} \rightarrow \mathrm{LiF} + (x-1)\mathrm{MF}_4 + \mathrm{MF}_3 + 2x\mathrm{H}_2\mathrm{O} \quad (4.5)$$

$$4x\mathrm{HF} + \mathrm{M}_x\mathrm{O}_{2x} \rightarrow x\mathrm{MF}_4 + 2x\mathrm{H}_2\mathrm{O} \qquad\qquad (4.6)$$

$$6\mathrm{HF} + \mathrm{Al}_2\mathrm{O}_3 \rightarrow 2\mathrm{AlF}_3 + 3\mathrm{H}_2\mathrm{O} \qquad\qquad (4.7)$$

Due to competing reactions (*e.g.*, reaction 4.2 and 4.5 – 4.7) in which both HF and H_2O might be generated and/or be consumed, it is challenging to precisely determine the extent of these acid-base reactions. As TMs located at the surface are more susceptible to nucleophilic attack by F$^-$, 25 % – 35 % of the total TMs present on the surface monolayer of the active materials directly exposed to the electrolyte are calculated to have dissolved.

In summary, Figure 4.6 illustrates a qualitative trend: (i) uncoated active materials released more TMs than coated, and (ii) delithiated active materials released more TMs than lithiated. When the active materials are in a delithiated state, coating is less efficient, despite a decrease in TM dissolution. The reduced concentrations of dissolved TM for coated active material might simply be due to HF attacking the alumina coating (*e.g.*, reaction 4.7), functioning as HF scavenger.[85] The alumina coating seems to be more effective for NMC than LMO, which might be due to the thicker coating produced on NMC (see Table 1 in **Paper IV**). The decreased alkalinity of Al_2O_3 and its lower tendency to produce H_2O dampen the auto-catalytic $LiPF_6$ degradation. Due to the reasonable decreased acidity of the predominating TM^{+2} and TM^{+3} at the surface, the lithiated active materials may have less vulnerability to nucleophilic attack by HF. Lithiated pristine NMC released almost entirely Mn, which is the only TM in a +IV oxidation state. Furthermore, the delithiated LMO (containing predominantly Mn^{+4}) released twice as much Mn as lithiated pristine LMO (containing an equal amount of Mn^{+3} and Mn^{+4}). The popular concept that Mn^{3+} is the most

sensitive to TM dissolution owing to the disproportionation reaction is thus implausible. Therefore, while disproportion reaction-based dissolution is possible, an acid-base/electrolyte-cathode founded dissolution mechanism explains the general TM dissolution observed in Li-ion cathodes.

4.2.3 Role of EC electrolyte solvent on TM dissolution

In addition to the chemical TM dissolution highlighted in the previous subsection and detailed in **Paper IV**, the electrode potential instigated dissolution of TM is assessed in **Paper V**. The focus here was on EC solvent, a typical component of an electrolyte solution used as co-solvent mixed with other types of carbonate-based solvents.

Numerous EC oxidation reaction routes have been proposed, including nucleophilic attack reactions involving oxides and carbonate molecules, electrophilic attack, and dehydrogenation processes.[124–126] Jung *et al.*[48] proposed a mechanism for EC dehydrogenation that generates protic species on the cathode surface, which may subsequently initiate the decomposition of $LiPF_6$ salt producing HF, transition metal fluorides (TMF_x), and PF_3O (see Figure 1.5, **section 1.4**). Zhang *et al.*[127] also reported that this mechanism of EC degradation-based on cathode surface oxygen is the most energetically favourable. Due to its high dielectric constant, which is important for dissociating Li-salts in solution, EC has been essential in organic liquid electrolytes for LIBs. Additionally, EC provides an efficient solid electrolyte interphase (SEI) on the typically utilized graphite anode.[128–130] In *lieu* of EC, several anodically stable fluorinated compounds, phosphates, and sulfones have been suggested as electrolyte components.[92,131–133] However, these alternative electrolyte systems have been demonstrated to have poor wettability, high viscosity and impedance, as well as significant cost and safety implications (*e.g.*, fluorinated solvents).[134,135] Sulfolane (tetramethylene sulfone, SL), despite its high viscosity, is a good alternative for replacing EC in the electrolyte solution, since the oxygen in the sulfolane group can coordinate with Li^+ to offer favourable conditions for salt dissolution. The absence of an O-H group in the structure also renders it less susceptible to the aforementioned dehydrogenation process.[90] Tilstam *et al.* among others have shown that SL is stable up to $E > 5.5$ V *vs.* Li/Li^+.[43,136] This set the basis for **Paper V**, which investigated the electrochemical performance and subsequent effect on TM dissolution of SL and DEC co-solvents in combination with LiBOB and $LiPF_6$ salts. However, evaluating the influence of SL on electrochemical performance with graphite, Li-metal, or other low-potential anode materials as the counter electrodes is problematic, since EC will certainly provide a better SEI formation. Similar to **Paper I**, **Paper V** addresses this issue by incorporating LFP as a counter electrode. The TM dissolution and HF evolution profile of NCA||LFP and LMO||LFP cells was investigated after 100 cycles. The cells contained $EC:DEC:LiPF_6$,

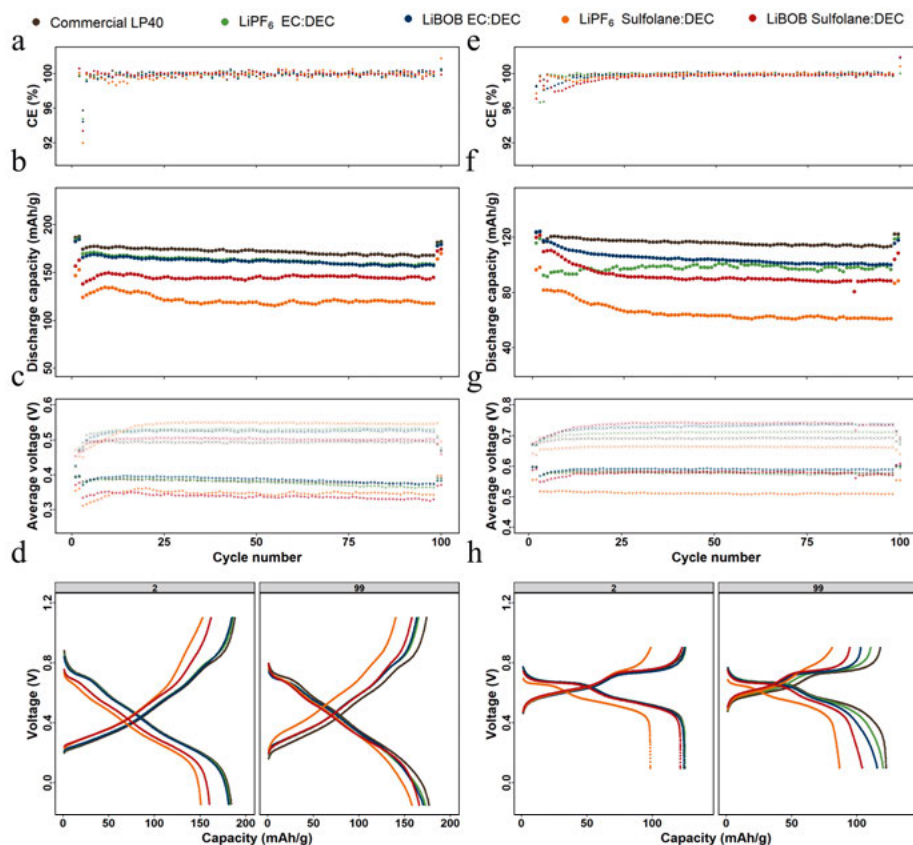EC:DEC:LiBOB, SL:DEC:LiPF$_6$ or SL:DEC:LiBOB electrolyte combinations, with a solvent ratio of 1:1 vol. %.

Figure 4.7. NCA|LFP cells with LiBOB and LiPF6 electrolytes in either EC|DEC or SL|DEC solvents are cycled for 100 cycles between the voltage window of 0.2 – 0.9 V (equivalent to 3.5 and 4.5 V vs. Li/Li$^+$), first and last two cycles at C/10 and the rest at 1C. (a) Coulombic efficiency. (b) Capacity retention. (c) Average voltage. (d) Voltage profile of the 2nd and 99th cycle. Corresponding LMO|LFP cells cycled for 100 cycles between 0.2 – 0.9 V (equivalent to 3.5 and 4.3 V vs. Li/Li$^+$), first and last two cycles at C/10 and the rest at 1C. (e) Coulombic efficiency. (f) Capacity retention. (g) Average voltage. (h) Voltage profile of the 2nd and 99th cycle.

Figure S1 of **Paper V** illustrates the ionic conductivity, H$_2$O concentration from coulometric KF measurements, and HF content of the investigated electrolytes. At temperatures ranging from 30 °C to 60 °C, EC-based electrolytes have consistently higher ionic conductivity than SL-based electrolytes. Similarly, electrolytes containing LiPF$_6$ have higher ionic conductivity than electrolytes containing LiBOB. Electrochemical cycling of LMO‖LFP and NCA‖LFP showed that the initial discharge capacities of the prepared electrolytes increase in the order of LiPF$_6$:SL:DEC, LiBOB:SL:DEC, LiBOB:EC:DEC, and

47

LiPF$_6$:EC:DEC, for both NCA||LFP and LMO||LFP cells ([Figure 4.7](#)). Figure 4.7 also demonstrates that SL-based electrolytes show higher polarisation, which is paralleled by capacity fade. In addition to the clear discrepancy in bulk ionic conductivity, this indicates that the electrode/electrolyte interphase layer formed in EC-based electrolytes is more conductive for Li$^+$ transport than in SL-based electrolytes. The capacity loss for the EC-based electrolytes of LiPF$_6$ and LiBOB in LMO||LFP cells was 3.5% and 4.9%, respectively, compared to 4.4% and 9.6% for the SL-based electrolytes of the same salts.
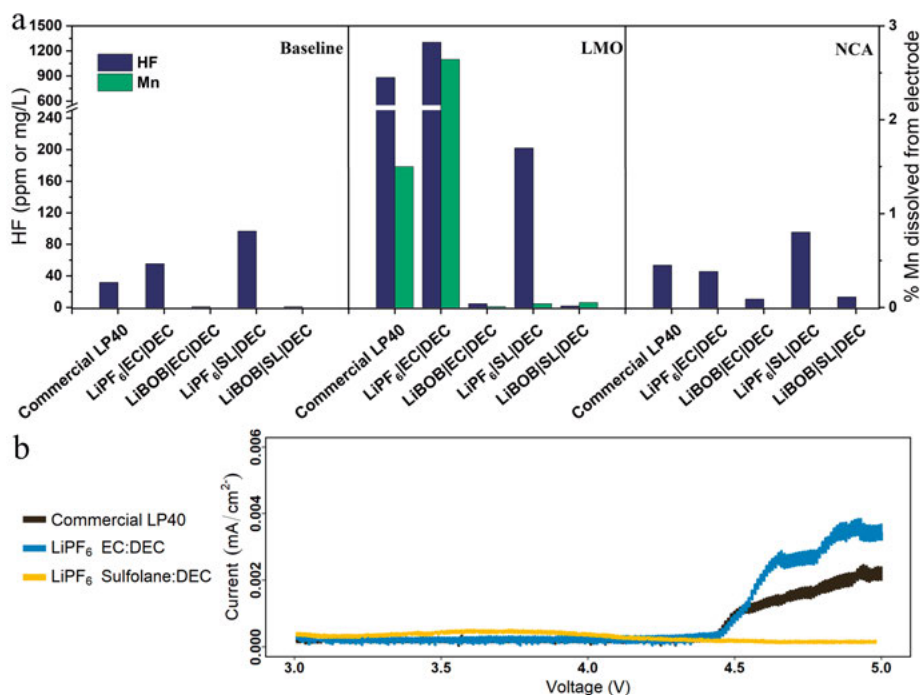

Figure 4.8. (a) Measured HF in the electrolyte and %Mn dissolved into the electrolyte after 100 cycles. Baseline (uncycled electrolyte). (b) PITT characterization of commercial LP40, LiPF$_6$:EC:DEC and LiPF$_6$:SL:DEC electrolytes. Carbon coated Al electrodes were cycled up to 5 V vs. Li/Li$^+$.

As illustrated in [Figure 4.8a](#), electrolytes collected from cycled LMO||LFP and NCA||LFP cells, as well as electrolytes stored free of active materials for the length of the experiment ("Baseline"), were analysed using ICP and F$^-$ probe. The HF concentration in the LMO cells clearly increases after cycling; however, for NCA cells is almost the same as Baseline. The presence of LiPF$_6$ in the electrolytes can specifically be correlated to the detection of HF. The highest HF concentration is 1304 ppm in the prepared LiPF$_6$:EC:DEC for LMO, followed by commercial LP40 at 880 ppm. Despite the fact that the prepared LiPF$_6$:EC:DEC electrolyte had 0.7 M LiPF$_6$ compared to the commercial LP40

electrolyte's 1 M $LiPF_6$, it generated more HF after cycling. This is due to the higher concentration of H_2O impurity, (see Figure S1 in **Paper V**). HF is detected SL-based cells containing $LiPF_6$, although at lower levels of 202 ppm for LMO and 95 ppm for NCA. When both $LiPF_6$ and EC are present in the electrolyte, LMO‖LFP cells generate an order of magnitude higher HF concentration than NCA‖LFP cells. The electrode surface and electrolyte contact differ due to the difference in specific surface area between NCA (0.36 m^2/g) and LMO (1.86 m^2/g). Thus, the above discussed EC dehydrogenation mechanism transpires to a larger extent in LMO cells. This is mirrored in the TM dissolution characteristics of both materials, with LMO‖LFP cells displaying Mn dissolution exclusively in the case of EC-based cells containing $LiPF_6$ whereas NCA shows no TM dissolution. Due to an increase in acidic species generated from electrolyte degradation, the onset of TM dissolution in Ni-rich layered oxides is $E > 4.5$ V $vs.$ Li/Li^+. Thus, TM dissolution for NCA in **Paper V** will be limited.[95,96]

According to the chemical dissolution profiles of LMO and NMC discussed in **subsection 4.2.2** (detailed in **Paper IV**), the HF concentration decreases when the electrolyte encounters the active materials owing to an acid-base interaction (Figure 4.6). In contrast, **Paper V** demonstrates for LMO that the HF increases when the electrolyte encounters active materials under electrochemical cycling conditions ((Figure 8a). This indicates that HF is also generated through an oxidative degradation of EC and casts doubt on the stability of EC. PITT measurements (Figure 4.8b) contrasting $LiPF_6$:EC:DEC and $LiPF_6$:SL:DEC electrolytes support this observation. The EC-based electrolyte starts to pass charge just below 4.4 V $vs.$ Li/Li^+, whereas the SL-based electrolyte remains stable up to 5 V $vs.$ Li/Li^+. This is not reflected, however, in the cycling performance of SL-based electrolytes, which exhibit higher polarisation and lower initial capacities. This highlights the significance of the CEI layer and ionic conductivity, at which EC-based electrolytes in relative tend to excel. Thus, while SL-based electrolytes conform to a desired structural property at high potentials by limiting further HF generation and restricting TM dissolution, they are less capable of supporting Li^+ transport at the cycling conditions tested in **Paper V**.

4.2.4 Role of an electrolyte additive ($LiPF_2O_2$) on TM dissolution

As discussed in previous subsections, electrolytes containing EC co-solvent and $LiPF_6$ conducting salt have been shown to degrade at high voltages, with significant gas generation and cell impedance increase, as well as the reported TM dissolution in this thesis.[54] The use of suitable electrolyte additives is a technologically and economically beneficial strategy for optimizing the interaction between the alkaline cathode and the acidic electrolyte. One interesting additive that has lately garnered attention is lithium difluoro phosphate ($LiPO_2F_2$, LiDFP). It is proposed to contribute to the formation of a stable interface with the electrolyte on both the cathode and anode surfaces.[139,140] Difluoro-phosphate ($PO_2F_2^-$) undergoes hydrolysis in the presence of trace amounts of H_2O in the electrolyte, resulting in the formation of LiF and Li_3PO_4 (reaction 4.8).[141] Klein *et al.* suggested that the presence of Li_3PO_4 degradation product from reaction 4.8 could act as a 'scavenging' agent for dissolved TM-ions, forming insoluble $TM-PO_4$ compounds and reducing TM crossover to the anode.[142] Following an acid-base interaction (electrolyte-cathode), as discussed in **Paper IV**, the dissolution of TM will invariably lead to the formation of H_2O (reaction 4.5). As a result, the presence of H_2O should continue to drive the hydrolysis of both $LiPF_6$ and $LiPO_2F_2$, increasing the HF concentration in the electrolyte (reaction 4.1 and 4.2). LiDFP is also reported to contribute to a reduction in TM dissolution from the cathode. However, the consensus is that it does not prevent TM dissolution. In addition, previous investigations on the benefits of LiDFP for TM dissolution had solely focused on characterization of the counter electrode. **Paper VI** investigates the effect of LiDFP as an additive on TM dissolution and cycling stability of NMC622 *vs.* graphite full-cells cycled at two upper cutoff voltages of 4.3 V and 4.6 V.

$$2H_2O + PO_2F_2^- \rightarrow Li_3PO_4 + LiF\ +\ HF +\ 3H^+ \tag{4.8}$$

Figure 4.9 shows the electrochemical cycling stability of "Baseline" (LP40 with no additive) and "LIDFP" (LP40 with 0.75 % LiDFP) electrolytes in NMC622 *vs.* graphite cells. The potential profiles of both electrolytes are highly comparable in the initial cycles and exhibit a large overlap in both cut-off voltages. All the cells showed low rate capability, with capacity dropping at 1C due to the high mass loading of the electrodes chosen (see experimental section of **Paper VI**). The intermittently high C-rate cycling protocol simulates commercial operating conditions of the cells, and the large cathode mass loading assures that any potential TM dissolution in the electrolyte is greater than the ICP-OES lower concentration detection limit (100 ppb). For reference, Figure S1 in **Paper VI** illustrates a consistent capacity degradation in NMC622 *vs.* graphite full-cell cycled at C/3 and 4.6 V cut-off voltage. At 4.2 V, the initial discharge capacities of LiDFP and Baseline are 176 mAh/g and 175 mAh/g, respectively (see Figure 4.9). Both electrolytes showed a comparable capacity retention of

84 %, over 100 cycles. Furthermore, at 1C, the charge/discharge polarisation for both electrolytes is shown to be constant at 250 mV. Thus, the additive does not introduce any positive or negative contributions at 4.2 V. At 4.6 V, however, the polarisation of the Baseline electrolyte significantly increases, in contrast to that of LiDFP. For LiDFP and Baseline, the polarisation is about 300 mV in the first 50 cycles (at 1C), but it increases after 50 cycles for baseline compared to LiDFP, where 600 mV and 1 V are recoded at the 99th cycle, respectively. Furthermore, the cell containing LiDFP has an improved capacity retention of 67 % as compared to the Baseline of 56 %. This suggests a contribution to a more efficient SEI/CEI formation for the LiDFP electrolyte.

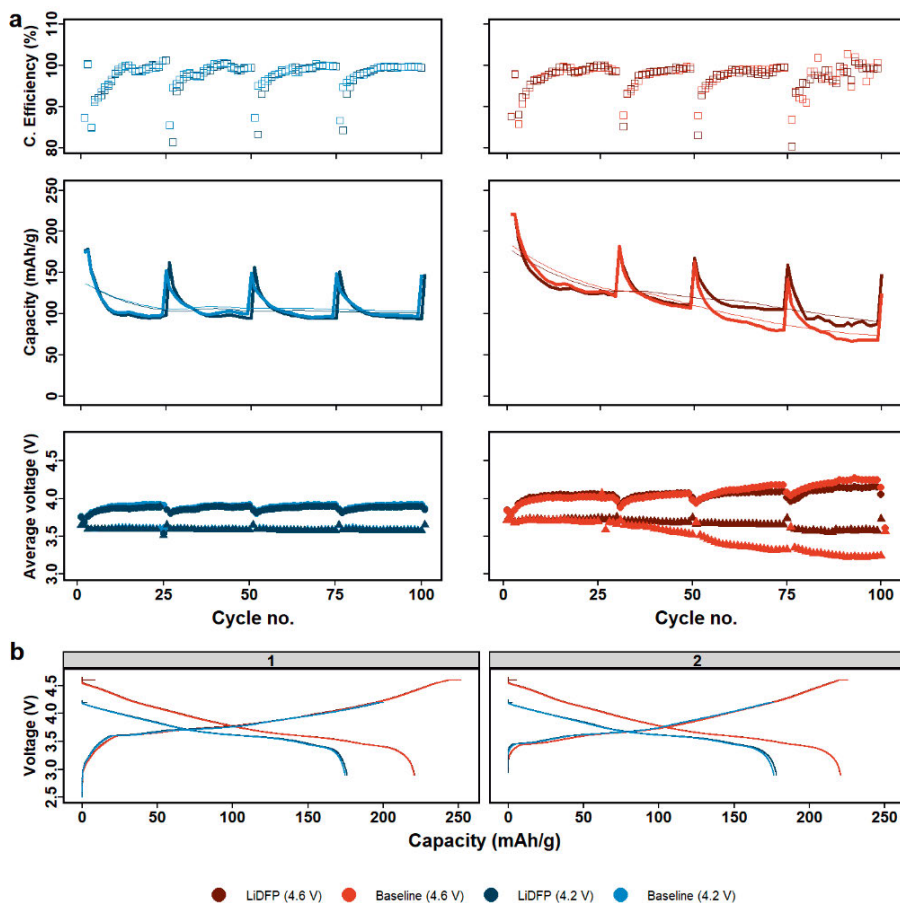Figure 4.9. (a) Electrochemical performance of NMC622-graphite full-cells using LP40 electrolyte without electrolyte additive (Baseline) and 0.75 wt. % LiDFP additive cycled for 100 cycles in the voltage window of 2.9 V – 4.2 V and 2.9 V – 4.6 V. First and last two cycles at C/10 and the rest at 1C. C-rate is decrease to C/10 every 25 cycles to check capacity recovery. (b) 1st and 2nd cycle voltage profiles of cells in (a).

The XPS spectra of the analysed graphite electrodes after 100 cycles showed that the SEI composition did not differ significantly between the two electrolytes (see Figure 3 in **Paper VI**). Since rinsing electrodes before XPS measurement increases the risk of removing the deposited TM on the graphite surface, electrodes were unwashed prior to measurement. Therefore, signal from traces of LiPF$_6$ was accentuated in Li 1s, P 2p, and F 1s spectra. Despite this, electrodes cycled at 4.2 V had lower electrolyte degradation products on the surface, which correlates to the decreased polarisation seen in the electrochemical cycling. Figure 4.10 presents the ICP-OES and F$^-$ probe measurements of electrolytes recovered from cycled cells, electrolytes maintained free of contact with active materials throughout the experiment ("aged"), and electrolytes immediately after preparation ("fresh"). When the electrolytes come in contact with the electrodes (cycled electrolyte), HF concentration decreases. This contrasts to the HF increase observed in **Paper V** (Figure 4.8). However, in **Paper V**, LFP is used as a counter electrode, while graphite is used in here (**Paper VI**). This attests to the consumption of HF by the graphite surface, resulting in fluorinated SEI species (see Figure 3 in **Paper V**).
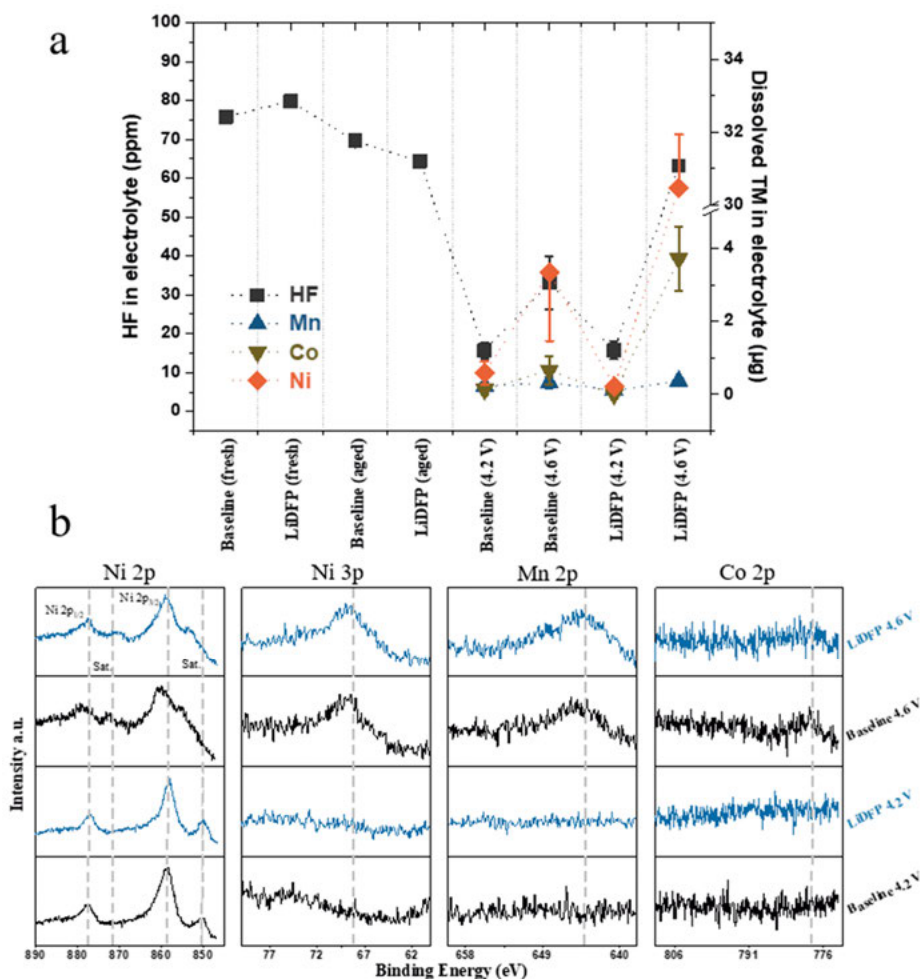
Figure 4.10. (a) Measured HF concentration in the electrolyte (quantified with a F⁻ selective electrode) and TM dissolved into the electrolyte (quantified by ICP-OES) after 100 cycles for the cells without additive (Baseline) and with 0.75 wt.% LiDFP electrolyte additive. HF concentration in electrolytes after preparation (fresh) and electrolytes maintained free of contact with active materials for the course of the experiment (aged) are also displayed. (b) Ni 2p, Ni 3p, Mn 2p, and Co 2p core-level XP spectra of graphite electrodes after 100 cycles.

At 4.2 V, the cycled and extracted LIDFP and Baseline electrolytes show HF values of 15.8 ± 2.3 ppm and 15.68 ± 2.1 ppm, respectively. Although HF decreases as mentioned above, the cut-off voltage is insufficiently high to generate surplus HF in the electrolyte. At 4.6 V, however, both electrolytes have higher HF content than their 4.2 V equivalents, with LiDFP showing 63.17 ± 0.51 ppm and the Baseline showing 33.09 ± 6.79 ppm of HF. Hence, in addition to HF consumption by cell components, electrolyte oxidation/degradation and thus $LiPF_6$ degradation is prevalent at 4.6 V. The higher HF content for LiDFP

compared to Baseline can be attributed to probable additive hydrolysis following reaction 4.8, yet it is also matched by the TM concentration in the electrolyte. LiDFP and Baseline have Ni contents of 30.5 ± 1.5 µg and 3.4 ± 1.9 µg, respectively. Similarly, the Co content of the equivalent electrolytes is 3.7 ± 0.9 µg and 0.7 ± 0.4 µg, respectively. Since Mn content was close to the lower detection limit, concentration could not be accurately quantified in the electrolyte. TM dissolution was limited in cells cycled at 4.2 V.

Additionally, the deposition of TM on the surface of the graphite was analysed by XPS for comparison with the ICP measurement in the electrolyte. Ni 2p spectra exhibit two Ni $2p_{3/2}$ and $2p_{1/2}$ peaks at $\sim$858 eV and $\sim$877 eV, respectively, with satellite peaks at $\sim$852 eV and $\sim$873 eV. The satellite peak at $\sim$873 eV is only seen on electrodes cycled at 4.6 V, showing that Ni deposition is higher at 4.6 V, compared to 4.2 V. This is further supported by the presence of Ni 3p and Mn 2p peaks from the cells with 4.6 V but not from the ones with 4.2 V. Thus, TM dissolution is accelerated when the cutoff voltage is increased. Although Mn is not present in the electrolyte, it is clearly found on the surface of graphite (from the cells cycled to 4.6 V). This observation is consistent with previous reports on NMC *vs.* graphite cells showing preferential Mn depositon on the anode.[143] Co deposited on the graphite was not detectable in any of the samples. Li_3PO_4, as a degradation product of LiDFP, has been shown to scavenge Co^{2+}, Ni^{2+}, and Mn^{2+}, resulting in Co_2PO_4, Ni_2PO_4, and Mn_2PO_4 precipitates in a standard carbonate electrolyte (EC:EMC).[142] Thus, in the presence of LiDFP, the cations precipitate out of the electrolyte to remain on the surface of cathode or separator rather than migrate to the anode and deposit. This can limit the amount of TM on the SEI and lead to the formation of a more preferable SEI, which is mirrored in the electrochemical performance. Despite the fact that several LiDFP hydrolysis routes have been identified, with a slight rise in HF as a product and an increase in the presence of TM (most likely in the form of TM-PO_4) in the extracted electrolyte, reaction 4.8 supports our findings.[144–146]

5 Conclusion

This thesis has investigated ageing mechanisms of LIB cathodes, with a focus on TM dissolution and on strategies to mitigate the dissolution. The first half, based on **Papers I–IV**, considered the possibility of modifying the cathode surface by for example surface coating to supress TM dissolution. The latter half considered the TM dissolution mechanism from an electrolyte perspective since TM dissolution is a direct consequence of electrode/electrolyte interaction. This latter part, based on **Papers I** and **IV–VI**, thus explored the roles of various electrolyte components.

Papers I–III investigate how a thin layer Al_2O_3 and TiO_2 coating formed by ALD on numerous cathode materials affects electrochemical cycling. The various cathodes demonstrated a variety of trends from the contribution of oxide coatings to cycling stability. Capacity retention and overall cycling stability were increased by Al_2O_3 coating on LCO and NMC811, as well as TiO_2 coating on LNMO. On the other hand, Al_2O_3 coating on LMO and LNMO showed little to no improvement in this aspect. Additionally, the 20 cycle ALD coated LNMO with Al_2O_3 provided an example of the detrimental effects that a suboptimal coating could have on cathode surface. When cycled under adverse conditions for the electrolyte at the average potential of 4.7 V *vs.* Li/Li^+ and the temperature of 50 °C, the surface of the ALD-coated primary particles developed visible holes. Non-uniformity in the coating results in non-uniform Li^+ conduction pathways, with Li^+ primarily flowing in and out of particles at select and electrochemically active locations where the coating is thinner or absent. The effect is increased with thicker Al_2O_3 coatings, which naturally increase non-uniformity. This results in non-uniform ageing of the cathode surface (pinholes), making these active locations more vulnerable to acidic species or electrolyte leaching agents (*e.g.*, HF). Thus, the coating coverage on cathode particles should have a significant impact on electrochemical stability. Although ALD has been shown to produce excellent and consistent coatings on flat surfaces, it is challenging to maintain the same level of consistency when coating differing porous powders. This is demonstrated by the ability of the same ALD recipe to produce varied coating quality, as observed from the electrochemical characterization. Upon comparing Al_2O_3 and TiO_2 coatings on the same cathode material (LNMO) in **Papers II** and **III**, it is demonstrated that the more ionically conductive and thinner TiO_2 coating layer provides better cycling stability. This indicates that a slightly denser and thinner coating layer provides a

lower risk of non-uniformity and pinhole formation, and hence promotes a more uniform Li^+ diffusion during electrochemical cycling.

Papers I–III emphasize the significance of tailoring the coating procedure primarily based on the cathode material. Oxide coatings in general should be ultrathin (sub-nm), homogeneous, and conformal. This necessitates consideration of substrate or cathode parameters such as surface area, particle size distribution, and cathode crystal structure. Despite the large number of studies available over the last decade on the capability of oxide coatings to increase cycling performance, much remains unknown about the electrode-coatings optimum interfacial properties that contribute to this performance.

Paper IV demonstrated that when not subjected to electrochemical cycling, *i.e.* no Li^+ transport into or out of cathode particles, the presence of an oxide layer protects the cathode from the acidic environment consistently provided by the electrolytes. The protective contribution of the coating layer is valid even if the coating does not provide total particle coverage. The investigation of chemical TM dissolution from lithiated and delithiated cathode materials coated with Al_2O_3 revealed that (i) uncoated active materials released more TMs than coated active materials, and (ii) delithiated active materials released more TMs than lithiated active materials. Reduced TM dissolution from coated active materials is due to HF attacking the coating film, as evidenced by fluorination of the oxide coatings. The lower alkalinity of Al_2O_3 (relative to cathode materials) and lower proclivity to generate H_2O when reacted with HF limits the auto-catalytic salt degradation, culminating in the coating functioning as an HF scavenger. The lithiated active materials were also found to be less sensitive to nucleophilic attack by HF due to the significantly decreased acidity of the predominating lower TM oxidation state ($\leq +III$) at the surface. The broadly accepted idea that Mn^{3+} is the most sensitive species to TM dissolution due to its disproportionation reaction is thus demonstrated to only be a minor factor. A chemical dissolution mechanism based on acid-base/electrolyte-cathode interaction explains the general TM dissolution observed in Li-ion cathodes better.

Papers I and **V** demonstrate that the presence of $LiPF_6$, and hence HF, in the electrolyte is the principal cause of TM dissolution, and that regulating acidity in conventional carbonate-based electrolytes is crucial. **Paper V** also demonstrates that HF increases when the electrolyte comes into contact with active materials during electrochemical cycling. This indicates that in addition to the hydrolysis of $LiPF_6$ leading to the formation of HF, HF is also generated through the oxidative degradation of EC. Despite the fact that TM dissolution is a chemical process, acidification of the electrolyte caused by oxidative degradation products also adds to the acceleration of TM dissolution. However, while replacing EC with an anodically stable solvent (SL) could minimize HF generation and TM dissolution, SL was demonstrated to be less capable of supporting Li^+ transport at the conditions studied in **Paper V**. Although $LiPF_6$ and EC have been found to be detrimental in terms of contributing to TM dissolu-

tion, considerable caution should be taken when attempting to replace the components, as a gain in preventing TM dissolution can come at the expense of electrochemical cycling performance. **Paper VI** introduced LiDFP electrolyte additive without replacing $LiPF_6$ or EC with any other components. Li_3PO_4, a degradation product formed from LiDFP, may aid in the removal of dissolved TM by precipitating the cations in the form of TM-PO_4 on the surface of the cathode, and thus restricting TM migration and deposition on the anode.

TM dissolution is a direct consequence of cathode-electrolyte interaction, with implications not only for redox active material loss but also for the composition and stability of SEI at the counter electrode. Therefore, optimizing the interaction between the alkaline cathode and the acidic electrolyte by either adding protective surface coatings on the cathode or regulating electrolyte acidity with additives or substituting electrolyte components is crucial for achieving the requisite for high potential cathode for Li-ion batteries.

6 Populärvetenskaplig sammanfattning

Den snabba ökningen av växthusgasutsläpp i vår miljö har radikalt förändrat de globala temperaturerna och medför nya risker för människors hälsa och en rad andra viktiga samhälleliga sektorer, som t.ex. jordbruket. I Kyoto- och Parisavtalen fastställdes bland annat ett mål om att drastiskt minska utsläppen till atmosfären från fossila energikällor senast år 2060. 195 länder har förbundit sig att hålla den globala temperaturökningen väl under 2 °C över de förindustriella nivåerna från år 1750.[3] Det uppskattas att mänsklig verksamhet redan har orsakat cirka 1,0 °C av den globala uppvärmningen jämfört med de förindustriella nivåerna, och det beräknas att ökningen kommer att nå 1,5 °C före år 2050 om uppvärmningen fortsätter i nuvarande takt.[3] För att målet skall uppnås måste det ske en betydande förändring av hur energin frambringas och används internationellt. Målet kan förmodligen enbart uppnås genom storskalig integration av förnybara energikällor som till exempel sol- och vindkraft. Emellertid är förnybara energialternativ som kan ersätta de traditionella fossilbränslebaserade energikällorna intermittenta, och bör därför kombineras med lämpliga energilagringssystem. Det vanligaste energilagringsystemet för tillfället är batteriteknik. Användningsområdena för batterier omfattar elnät, transport, marin- och ubåtsverksamhet, flygverksamhet, bärbara elektroniska apparater, trådlösa nätverkssystem och många fler. Batterier har historiskt kunna erbjuda en lösning på de flesta utmaningar som det har ställts inför. Dock är en ständig vidareutveckling av batterityper av största betydelse för att uppfylla framtida standarder och behov i den växande globala ekonomin.

Ett batteri omvandlar kemisk energi till elektrisk energi genom en elektrokemisk reduktions- och oxidationsreaktion (redox-reaktion). Den elektriska energin kan utnyttjas när batteriet sätts i drift, och elektrisk energi kan lagras i form av kemisk energi när batteriet används som lagringsenhet. Under de senaste fyra decennierna har litiumjonbatterier (LIB) blivit mycket pålitliga elektrokemiska energilagringssystem på grund av deras relativt höga effekt- och energidensitet i jämförelse med alternativa batterikemier. Detta beror på att litium-jonen är liten och har hög elektropositivitet. De fyra huvudkomponenterna i ett LIB är katod, anod, elektrolyt och separator. Under elektrokemisk laddning vandrar litiumjonerna från katoden genom elektrolyten till anoden och vandrar sedan tillbaka under urladdningen. Grafit är för närvarande det mest populära materialet, men vissa batteritillverkare har valt icke-grafitanoder som litiumtitanat ($Li_4Ti_5O_{12}$). Litiumsalt och organiska (vanligtvis) lösningsmedel

utgör elektrolyten. Litiumhexafluorofosfat ($LiPF_6$) är det överläget mest använda saltet, men salter som litiumperklorat ($LiClO_4$) eller litiumbis(oxalato)borat (LiBOB) kan också förekomma. Det organiska lösningsmedlet är viktigt för att främja diffusionen av litiumjoner mellan elektroderna och är därför en kritisk komponent för batteriets effektivitet. Etylmetylkarbonat (EMC), dimetylkarbonat (DMC), dietylkarbonat (DEC), propylen karbonat (PC) och etylenkarbonat (EC) är några av de vanligaste karbonatbaserade organiska lösningsmedlen. Separatorn i sin tur är en säkerhetskomponent mellan katoden och anoden, som förhindrar direkt kontakt mellan elektroderna, eller kortslutning, medan den tillåter litiumjonerstransport. Polyeten och polypropen, eller en kombination av båda, är de vanligaste materialen som utgör separatorer.

Katoden, som utgör källan till litiumjoner, är huvudsakligen den elektrod som bestämmer egenskaperna hos ett LIB. Därför är befintliga kommersiella batterier ofta benämnda efter det material som denna komponent består av. Litiumkoboltoxid (LCO), litiummanganoxid (LMO), litiumjärnfosfat (LFP), litiumnickel-kobolt-aluminiumoxid (NCA) och litiumnickel-mangan-koboltoxid (NMC) är några av de kommersiellt och forskningsmässigt intressanta oxid- och fosfatkatoderna. Alla innehåller de redox-aktiva övergångsmetaller (TM). Energidensiteten hos nuvarande LIB:er begränsas av driftsspänningen och kapaciteten hos de katodmaterial som används. Vilket innebär ju högre katodpotentialen är, desto högre energidensiteten blir för batteriet. Dessutom begränsar den låga stabiliteten hos "konventionella" karbonatbaserade elektrolyter möjligheten att utvidga LIB-driftsspänningen. Upplösning av TM i elektrolyten medan batteriet är i drift är ett allvarligt problem som i hög grad bidrar till att LIB:er åldras. I avhandlingen undersöktes därför katoders åldringsmekanismer, med fokus på upplösning av TM och strategier för att begränsa upplösningsprocessen. I den första halvan av avhandlingen undersöktes en strategi av att modifiera katodytan genom ytbeläggning för att förhindra TM-upplösning. I den andra halvan av avhandlingen undersöktes TM-upplösningsmekanismen ur ett elektrolytperspektiv, eftersom TM-löslighet är en direkt konsekvens av växelverkan mellan katod och elektrolyt.

Från katodytans perspektiv har ALD-beläggning (atomlagerdeposition) på katodytan med elektroniskt isolerande Al_2O_3- och TiO_2-beläggningar undersökts som en strategi för att stabilisera gränssnittet mellan katod och elektrolyt och minimera upplösning av TM. När oxiderade TM-joner kommer i kontakt med de elektronrika elektrolytämnena i gränsskiktet mellan katod och elektrolyt (det så kallade CEI) genomgår de en irreversibel reduktionsreaktion. Dessa reduktionsreaktioner orsakar nedbrytning av elektrolyten samt en strukturell förändring av katodytan. Bildandet av en elektrokemiskt inert struktur på grund av denna förändring av ytan ökar impedansen hos katoden avsevärt. Oxidbeläggningarna är således designade för att fungera som en elektronisk barriär mot direktkontakt mellan elektrolyten och redox-aktiva TM-joner på katodytan. Avhandlingen illustrerar både fördelarna och begränsningarna av amorfa oxidbeläggningsmaterial under elektrokemisk cykling. Ultratunna oxidskikt

begränsar den autokatalytiska saltnedbrytningen och därmed ackumulationen av sura ämnen i elektrolyten, vilket innebär att beläggningen fungerar som ett skyddande skikt. En suboptimal beläggning bidrar å andra sidan till ett icke-homogent åldrande av katodytan, vilket har visat sig vara elektrokemiskt ofördelaktigt. Dessutom visar avhandlingen att en kemisk upplösningsmekanism baserad på interaktion mellan syra-bas/elektrolyt-katod ligger bakom den omfattande TM-löslighet som observerats i en del Li-jonkatoder.

Från elektrolytens perspektiv demonstrerar avhandlingen att $LiPF_6$, och därmed HF, är den huvudsakliga källan till upplösning av TM. Det är känt att vatten som förekommer i elektrolyten i små mängder kan hydrolysera $LiPF_6$-saltet i en sönderfallsreaktion som bildar HF. HF och liknande suraämnen i elektrolyten är synnerligen korrosiva mot katodytan och resulterar i TM-upplösning. Förutom hydrolys av $LiPF_6$ bidrar nedbrytningen av etylenkarbonat (EC) till ytterligare generering av HF. En ökning av nedbrytningsprodukter i elektrolyten accelererar följaktligen TM-upplösningen. Att (i) ersätta EC med ett mer oxidationsstabilt lösningsmedel (t.ex. tetrametylensulfon) (ii) ersätta $LiPF_6$ med ett icke-fluorerat salt (t.ex. LiBOB eller $LiClO_4$) eller (iii) tillsätta en kemisk förening som fångar upplösta TM t.ex. litiumdifluorofosfat ($LiPO_2F_2$, LiDFP) undersöktes i avhandlingen. Strategierna antingen i) begränsar upplösningen av TM, ii) förhindrar migration och deponering av TM på anodytan eller iii) förhindrar bildning av sura nedbrytningsprodukter i elektrolyten. Genom att ersätta EC med det mer oxidationsstabila lösningsmedlet SL och ersätta $LiPF_6$ med icke-fluoriderade salt ($LiClO_4$ eller LiBOB) begränsades HF-bildningen och TM-upplösningen. LiDFP bidrog till att eliminera TM genom att fälla ut de upplösta TM-katjonerna och på så sätt begränsa TM-migrationen och -depositionen på anodytan. Avhandlingen belyser dock behovet av att ta viss hänsyn vid försök av att utbyta elektrolytkomponenterna, eftersom en minskning av TM-upplösningen kan ske på bekostnad av elektrokemisk prestanda.

Interaktionen mellan katod och elektrolyt avgör TM-upplösningsprofilen i LIB:er, vilket inte bara innebär förlust av redox-aktivt material från katoden utan också inverkan på sammansättningen och stabiliteten hos gränsskiktet mellan elektrolyt och anod. Därför är det viktigt att optimera interaktionen mellan den alkaliska katoden och den sura elektrolyten genom antingen applicera skyddande ytbeläggningar på katoden eller genom att reglera elektrolytens surhetsgrad med hjälp av tillsatser eller genom att byta ut elektrolytkomponenter för att uppnå den höga arbetspotential som fordras för katoden i litiumjonbatterier.

7 Acknowledgement

First and foremost, I'd like to thank Reza, my main supervisor. I am extremely grateful for your guidance and support over the years, as well as for introducing me to the world of batteries so long ago now. I am also grateful to Erik, my co-supervisor, for your research advice and guidance. I also want to thank Haidong, my unofficial supervisor in the last year. Your attention to detail is unparalleled, and it is something I will retain for the future.

I'd like to express my appreciation to Elise, my co-author. I've had a great time working with you. Certainly, for the rest of my co-authors, regardless of whether you worked on the projects listed in this thesis or not, it has been fruitful, insightful, and so much fun. I hope we can collaborate again in some capacity. I'd like to thank Erik, Mats, and Mårten for allowing me access and introducing me to ALD. I'd also like to thank Ronnie and Habtom; to say I've learned a lot from our discussions would be an understatement.

Thank you, Alina and Fredrik, for keeping the lab running. Alina, I will truly miss the random conversations that begin with gloveboxes or chemicals and end up on who knows what topic.

As a shockingly awful "plant keeper", my office plants perfectly define my relationship with you my office mates. I bring the plants with the expectation that they will only survive due to your presence. The plants have survived! Sincerely, Isabella, Tati, Robin, and Leon, it has been a joy sharing an office with you. Ålcoholics! It's been a pleasure to share so many wonderful memories in and out of Ångan!

As I mentioned in my Lice, I continue to hold the following sentiment: There are so many past and present members of the structural chemistry group I must thank. That, however, was what made my time here the most pleasant. It's the fact that I got to meet and talk with people from all walks of life, backgrounds, and parts of the world who have at least one thing in common with me. I'm still sceptical that I'll be able to get this experience elsewhere. Because our group has grown so large, I will personally thank each and every one of you, as many of you current and past group members have had such an impact on my time here.

Finally, to family and friends in Sweden and all over the world honestly. We're a big family, and I'm proud to have you all. ገዘና ከኣ፣ ዋ ነህለናልኩም ዶክቶረ ዮናስ ወዲ ሃይለ ናይ ቲኩል ፍረ ቃኛው ካብ ላልምባ (ትኩል)ን ጋብሩ(ኣፈልባ)ን ምስ ዮበልን ኣበልን ዮኣልን ናይ ቲኩል ፍረ ቃኛው፦ ቱታ፦ :)

8 References

1.   Romero, J. P. & Gramkow, C. Economic complexity and greenhouse gas emissions. *World Dev.* **139**, (2021).
2.   Wright, V. P. WORLD ENERGY OUTLOOK. in 23–28 (1986).
3.   Jarraud, M. & Steiner, A. Summary for policymakers. *Managing the Risks of Extreme Events and Disasters to Advance Climate Change Adaptation: Special Report of the Intergovernmental Panel on Climate Change* vol. 9781107025 3–22 (2012).
4.   Sekai, K. *et al.* Lithium-ion rechargeable cells with LiCoO2 and carbon electrodes. *J. Power Sources* **43**, 241–244 (1993).
5.   Goodenough, J. B. & Park, K. S. The Li-ion rechargeable battery: A perspective. *Journal of the American Chemical Society* vol. 135 1167–1176 (2013).
6.   Liu, C., Neale, Z. G. & Cao, G. Understanding electrochemical potentials of cathode materials in rechargeable batteries. *Materials Today* vol. 19 109–123 (2016).
7.   Robert, R., Bunzli, C., Berg, E. J. & Novák, P. Activation Mechanism of LiNi0.80Co0.15Al0.05O2: Surface and bulk operando electrochemical, differential electrochemical mass spectrometry, and x-ray diffraction analyses. *Chem. Mater.* **27**, 526–536 (2015).
8.   Mizushima, K., Jones, P. C., Wiseman, P. J. & Goodenough, J. B. LixCoO2 (0<x≤1): A new cathode material for batteries of high energy density. *Solid State Ionics* **3**–**4**, 171–174 (1981).
9.   Antolini, E. LiCoO2: Formation, structure, lithium and oxygen nonstoichiometry, electrochemical behaviour and transport properties. *Solid State Ionics* **170**, 159–171 (2004).
10.   Amatucci, G. G., Tarascon, J. M. & Klein, L. C. Cobalt dissolution in LiCoO2-based non-aqueous rechargeable batteries. *Solid State Ionics* **83**, 167–173 (1996).
11.   Chen, Z. & Dahn, J. R. Methods to obtain excellent capacity retention in LiCoO2 cycled to 4.5 V. *Electrochim. Acta* **49**, 1079–1090 (2004).
12.   Sverdrup, H. U., Ragnarsdottir, K. V. & Koca, D. Integrated Modelling of the Global Cobalt Extraction, Supply, Price and Depletion of Extractable Resources Using the WORLD6 Model. *Biophys. Econ. Resour. Qual.* **2**, 4 (2017).
13.   Sovacool, B. K. The precarious political economy of cobalt: Balancing prosperity, poverty, and brutality in artisanal and industrial mining in the Democratic Republic of the Congo. *Extr. Ind. Soc.* **6**, 915–939 (2019).
14.   Dahn, J. R., von Sacken, U. & Michal, C. A. Structure and electrochemistry of Li1±yNiO2 and a new Li2NiO2 phase with the Ni (OH)2 structure. *Solid State Ionics* **44**, 87–97 (1990).

15. Dutta, G., Manthiram, A., Goodenough, J. B. & Grenier, J. C. Chemical synthesis and properties of Li1-δ-xNi1+δO2 and Li[Ni2]O4. *J. Solid State Chem.* **96**, 123–131 (1992).

16. Davidson, I., Greedan, J. E., von Sacken, U., Michal, C. A. & Dahn, J. R. Structure of 1T-Li2NiO2 from powder neutron diffraction. *Solid State Ionics* **46**, 243–247 (1991).

17. Delmas, C., Saadoune, I. & Rougier, A. The cycling properties of the LixNi1-yCoyO2 electrode. *J. Power Sources* **44**, 595–602 (1993).

18. Rougier, A., Gravereau, P. & Delmas, C. Optimization of the Composition of the Li[sub 1−z]Ni[sub 1+z]O[sub 2] Electrode Materials: Structural, Magnetic, and Electrochemical Studies. *J. Electrochem. Soc.* **143**, 1168 (1996).

19. Armstrong, A. R. & Bruce, P. G. Synthesis of layered LiMnO2 as an electrode for rechargeable lithium batteries. *Nature* **381**, 499–500 (1996).

20. Gummow, R. J., Liles, D. & Thackeray, M. Lithium extraction from orthorhombic lithium manganese oxide and the phase transformation to spinel. *Mater. Res. Bull.* **28**, 1249–1256 (1993).

21. Ohzuku, T. & Makimura, Y. Layered lithium insertion material of LiCo1/3Ni1/3Mn1/3O2 for lithium-ion batteries. *Chem. Lett.* **30**, 642–643 (2001).

22. Kim, J.-M. & Chung, H.-T. The first cycle characteristics of Li[Ni 1/3 Co 1/3 Mn 1/3]O 2 charged up to 4.7 V. *Electrochim. Acta* **49**, 937–944 (2004).

23. Huang, Y. Q., Guo, W. Y., Li, D. C., Peng, Z. H. & Zhou, Y. H. Synthesis and electrochemical performance of LiNi1-xCo xO2 cathode materials for lithium ion batteries. *Chinese J. Inorg. Chem.* **21**, 736–740 (2005).

24. Chen, Z., Qin, Y., Amine, K. & Sun, Y. K. Role of surface coating on cathode materials for lithium-ion batteries. *J. Mater. Chem.* **20**, 7606–7612 (2010).

25. Kim, J. H., Ryu, H. H., Kim, S. J., Yoon, C. S. & Sun, Y. K. Degradation Mechanism of Highly Ni-Rich Li[NixCoyMn1- x- y]O2 Cathodes with x > 0.9. *ACS Appl. Mater. Interfaces* **11**, 30936–30942 (2019).

26. Schipper, F. *et al.* Review-Recent advances and remaining challenges for lithium ion battery cathodes I. Nickel-rich, LiNixCoyMnzO2. in *Journal of the Electrochemical Society* vol. 164 A6220–A6228 (Electrochemical Society Inc., 2017).

27. Park, K. J. *et al.* High-Capacity Concentration Gradient Li[Ni0.865Co0.120Al0.015]O2 Cathode for Lithium-Ion Batteries. *Adv. Energy Mater.* **8**, (2018).

28. Liang, C. *et al.* Unraveling the Origin of Instability in Ni-Rich LiNi1-2xCoxMnxO2 (NCM) Cathode Materials. *J. Phys. Chem. C* **120**, 6383–6393 (2016).

29. Noh, H. J., Youn, S., Yoon, C. S. & Sun, Y. K. Comparison of the structural and electrochemical properties of layered Li[NixCoyMnz]O2 (x = 1/3, 0.5, 0.6, 0.7, 0.8 and 0.85) cathode material for lithium-ion batteries. *J. Power Sources* **233**, 121–130 (2013).

30. Thackeray, M. M., David, W. I. F., Bruce, P. G. & Goodenough, J. B. c. *Mater. Res. Bull.* **18**, 461–472 (1983).

31. Aurbach, D. *et al.* Capacity fading of LixMn2O4 spinel electrodes studied by XRD and electroanalytical techniques. *J. Power Sources* **81**–**82**, 472–479 (1999).

32. Julien, C. M. & Mauger, A. Review of 5-V electrodes for Li-ion batteries: status and trends. *Ionics (Kiel).* **19**, 951–988 (2013).

33. Schipper, F. *et al.* Study of cathode materials for lithium-ion batteries: Recent progress and new challenges. *Inorganics* vol. 5 32 (2017).

34. Kuppan, S., Xu, Y., Liu, Y. & Chen, G. Phase transformation mechanism in lithium manganese nickel oxide revealed by single-crystal hard X-ray microscopy. *Nat. Commun.* **8**, (2017).

35. Schweidler, S. *et al.* Volume Changes of Graphite Anodes Revisited: A Combined Operando X-ray Diffraction and in Situ Pressure Analysis Study. *J. Phys. Chem. C* **122**, 8829–8835 (2018).

36. Edström, K., Gustafsson, T. & Thomas, J. O. The cathode-electrolyte interface in the Li-ion battery. in *Electrochimica Acta* vol. 50 397–403 (2004).

37. Peled, E. & Menkin, S. Review—SEI: Past, Present and Future. *J. Electrochem. Soc.* **164**, A1703–A1719 (2017).

38. Aurbach, D., Zinigrad, E., Cohen, Y. & Teller, H. A short review of failure mechanisms of lithium metal and lithiated graphite anodes in liquid electrolyte solutions. in *Solid State Ionics* vol. 148 405–416 (2002).

39. Aurbach, D. Electrode-solution interactions in Li-ion batteries: A short summary and new insights. in *Journal of Power Sources* vols 119–121 497–503 (2003).

40. Kawamura, T., Okada, S. & Yamaki, J. ichi. Decomposition reaction of LiPF6-based electrolytes for lithium ion cells. *J. Power Sources* **156**, 547–554 (2006).

41. Park, M. S. *et al.* A highly reversible lithium metal anode. *Sci. Rep.* **4**, (2014).

42. Xing, L., Vatamanu, J., Borodin, O., Smith, G. D. & Bedrov, D. Electrode/electrolyte interface in sulfolane-based electrolytes for Li ion batteries: A molecular dynamics simulation study. *J. Phys. Chem. C* **116**, 23871–23881 (2012).

43. Tilstam, U. Sulfolane: A versatile dipolar aprotic solvent. *Organic Process Research and Development* vol. 16 1273–1278 (2012).

44. Aurbach, D. *et al.* Recent studies on the correlation between surface chemistry, morphology, three-dimensional structures and performance of Li and Li-C intercalation anodes in several important electrolyte systems. *J. Power Sources* **68**, 91–98 (1997).

45. Aurbach, D. *et al.* Design of electrolyte solutions for Li and Li-ion batteries: A review. in *Electrochimica Acta* vol. 50 247–254 (Pergamon, 2004).

46. Sångeland, C. Exploring the Frontiers of Polymer Electrolytes for Battery Applications: From Surface to Bulk. (2021).

47. Kotronia, A. *Probing Critical Interfaces in Dual- Ion Batteries The Road Towards Performant Graphite Cathodes*. (2021).

48. Jung, R., Metzger, M., Maglia, F., Stinner, C. & Gasteiger, H. A. Oxygen Release and Its Effect on the Cycling Stability of LiNi x Mn y Co z O 2 (NMC) Cathode Materials for Li-Ion Batteries. *J. Electrochem. Soc.* **164**, A1361–A1377 (2017).

49. Wang, H. *et al.* Understanding the effects of surface reconstruction on the electrochemical cycling performance of the spinel LiNi0.5Mn1.5O4 cathode material at elevated temperatures. *J. Mater. Chem. A* **5**, 822–834 (2017).

50. Amos, C., Roldan, M. A., Varela, M., Goodenough, J. B. & Ferreira, P. J. Understanding the Surface Structure of LiMn2O4 Spinel Cathodes with Aberration-Corrected HAADF STEM and EELS. *Microsc. Microanal.* **21**, 1375–1376 (2015).

51. Lin, F. *et al.* Surface reconstruction and chemical evolution of stoichiometric layered cathode materials for lithium-ion batteries. *Nat. Commun.* **5**, 3529 (2014).

52. Watanabe, S., Kinoshita, M., Hosokawa, T., Morigaki, K. & Nakura, K. Capacity fade of LiAlyNi1-x-yCoxO 2 cathode for lithium-ion batteries during accelerated calendar and cycle life tests (surface analysis of LiAlyNi1-x-yCo xO2 cathode after cycle tests in restricted depth of discharge ranges). *J. Power Sources* **258**, 210–217 (2014).

53. Wandt, J., Freiberg, A. T. S., Ogrodnik, A. & Gasteiger, H. A. Singlet oxygen evolution from layered transition metal oxide cathode materials and its implications for lithium-ion batteries. *Mater. Today* **21**, 825–833 (2018).

54. Yu, Y. *et al.* Coupled LiPF6 Decomposition and Carbonate Dehydrogenation Enhanced by Highly Covalent Metal Oxides in High-Energy Li-Ion Batteries. *J. Phys. Chem. C* **122**, 27368–27382 (2018).

55. Azcarate, I. *et al.* Assessing the Oxidation Behavior of EC:DMC Based Electrolyte on Non-Catalytically Active Surface. *J. Electrochem. Soc.* **167**, 080530 (2020).

56. Zhang, Y. *et al.* Revealing electrolyte oxidation: Via carbonate dehydrogenation on Ni-based oxides in Li-ion batteries by in situ Fourier transform infrared spectroscopy. *Energy Environ. Sci.* **13**, 183–199 (2020).

57. Pieczonka, N. P. W. *et al.* Understanding transition-metal dissolution behavior in LiNi 0.5Mn1.5O4 high-voltage spinel for lithium ion batteries. *J. Phys. Chem. C* **117**, 15947–15957 (2013).

58. Imhof, R. & Novák, P. Oxidative electrolyte solvent degradation in lithium-ion batteries - An in situ differential electrochemical mass spectrometry investigation. *J. Electrochem. Soc.* **146**, 1702–1706 (1999).

59. Metzger, M., Strehle, B., Solchenbach, S. & Gasteiger, H. A. Origin of H 2 Evolution in LIBs: H 2 O Reduction vs. Electrolyte Oxidation. *J. Electrochem. Soc.* **163**, A798–A809 (2016).

60. Zhan, C., Wu, T., Lu, J. & Amine, K. Dissolution, migration, and deposition of transition metal ions in Li-ion batteries exemplified by Mn-based cathodes-A critical review. *Energy and Environmental Science* vol. 11 243–257 (2018).

61. Nordh, T. *et al.* Manganese in the SEI Layer of Li4Ti5O12 Studied by Combined NEXAFS and HAXPES Techniques. *J. Phys. Chem. C* **120**, 3206–3213 (2016).

62. Klein, S. *et al.* Re-evaluating common electrolyte additives for high-voltage lithium ion batteries. *Cell Reports Phys. Sci.* **2**, (2021).

63. Tsunekawa, H. *et al.* Capacity Fading of Graphite Electrodes Due to the Deposition of Manganese Ions on Them in Li-Ion Batteries. *J. Electrochem. Soc.* **149**, A1326 (2002).

64. Zhan, C., Qiu, X., Lu, J. & Amine, K. Tuning the Mn Deposition on the Anode to Improve the Cycle Performance of the Mn-Based Lithium Ion Battery. *Adv. Mater. Interfaces* **3**, 1500856 (2016).

65. Zhan, C., Wu, T., Lu, J. & Amine, K. Dissolution, migration, and deposition of transition metal ions in Li-ion batteries exemplified by Mn-based cathodes-A critical review. *Energy and Environmental Science* vol. 11 243–257 (2018).

66. Solchenbach, S., Hong, G., Freiberg, A. T. S., Jung, R. & Gasteiger, H. A. Electrolyte and SEI Decomposition Reactions of Transition Metal Ions Investigated by On-Line Electrochemical Mass Spectrometry. *J. Electrochem. Soc.* **165**, A3304–A3312 (2018).

67. Wang, C. *et al.* Overlooked electrolyte destabilization by manganese (II) in lithium-ion batteries. *Nat. Commun.* **10**, 3423 (2019).

68. Kim, Y., Lim, J. & Kang, S. Investigation on the dissolution of Mn ions from LiMn2O 4 cathode in the application of lithium ion batteries: First principle molecular orbital method. *Int. J. Quantum Chem.* **113**, 148–154 (2013).

69. Arora, P., White, R. E. & Doyle, M. Capacity fade mechanisms and side reactions in lithium-ion batteries. *J. Electrochem. Soc.* **145**, 3647–3667 (1998).

70. Aoshima, T., Okahara, K., Kiyohara, C. & Shizuka, K. Mechanisms of manganese spinels dissolution and capacity fade at high temperature. in *Journal of Power Sources* vols 97–98 377–380 (2001).

71. Cai, L. *et al.* Life modeling of a lithium ion cell with a spinel-based cathode. *J. Power Sources* **221**, 191–200 (2013).

72. Xia, Y., Zhou, Y. & Yoshio, M. Capacity fading on cycling of 4 V Li/LiMn2O4 cells. *J. Electrochem. Soc.* **144**, 2593–2600 (1997).

73. Lu, J. & Lee, K. S. Spinel cathodes for advanced lithium ion batteries: a review of challenges and recent progress. *Materials Technology* vol. 31 628–641 (2016).

74. Yamada, A. Lattice instability in Li(LixMn2-x)O4. *J. Solid State Chem.* **122**, 160–165 (1996).

75. Li, X., Xu, Y. & Wang, C. Suppression of Jahn-Teller distortion of spinel LiMn2O4 cathode. *J. Alloys Compd.* **479**, 310–313 (2009).

76. Tarascon, J. M. & Guyomard, D. The Li1+xMn2O4/C rocking-chair system: a review. *Electrochim. Acta* **38**, 1221–1231 (1993).

77. Du Pasquier, A. *et al.* Mechanism for Limited 55°C Storage Performance of Li1.05 Mn1.95 O4 Electrodes. *J. Electrochem. Soc.* **146**, 428–436 (1999).

78. Amatucci, G. G., Blyr, A., Sigala, C., Alfonse, P. & Tarascon, J. M. Surface treatments of Li1+xMn2-xO4 spinels for improved elevated temperature performance. *Solid State Ionics* **104**, 13–25 (1997).

79. Nishimura, K. *et al.* Spinel-type lithium-manganese oxide cathodes for rechargeable lithium batteries. *J. Power Sources* **81**–**82**, 420–424 (1999).

80. Antonini, A., Bellitto, C., Pasquali, M. & Pistoia, G. Factors affecting the stabilization of Mn spinel capacity upon storing and cycling at high temperatures. *J. Electrochem. Soc.* **145**, 2726–2732 (1998).

81. Wachs, S. J. *et al.* Online Monitoring of Transition-Metal Dissolution from a High-Ni-Content Cathode Material. *ACS Appl. Mater. Interfaces* **13**, 33075–33082 (2021).

82. Edge, J. S. *et al.* Lithium ion battery degradation: what you need to know. *Physical Chemistry Chemical Physics* vol. 23 8200–8221 (2021).

83. Mattelaer, F., Vereecken, P. M., Dendooven, J. & Detavernier, C. The Influence of Ultrathin Amorphous ALD Alumina and Titania on the Rate Capability of Anatase TiO_2 and $LiMn_2O_4$ Lithium Ion Battery Electrodes. *Adv. Mater. Interfaces* **4**, 1601237 (2017).

84. Xiao, X., Lu, P. & Ahn, D. Ultrathin multifunctional oxide coatings for lithium ion batteries. *Adv. Mater.* **23**, 3911–3915 (2011).

85. Li, X. *et al.* Significant impact on cathode performance of lithium-ion batteries by precisely controlled metal oxide nanocoatings via atomic layer deposition. *J. Power Sources* **247**, 57–69 (2014).

86. Zhou, L. *et al.* Enhanced cycling stability and rate capability of Bi2O3-coated Li1.2Mn0.54Ni0.13Co0.13O2 cathode materials for lithium-ion batteries. *RSC Adv.* **6**, 69790–69797 (2016).

87. Sun, Y.-K., Cho, S.-W., Lee, S.-W., Yoon, C. S. & Amine, K. AlF[sub 3]-Coating to Improve High Voltage Cycling Performance of Li[Ni[sub 1⁄3]Co[sub 1⁄3]Mn[sub 1⁄3]]O[sub 2] Cathode Materials for Lithium Secondary Batteries. *J. Electrochem. Soc.* **154**, A168 (2007).

88. Deng, B. *et al.* Effects of Charge Cutoff Potential on an Electrolyte Additive for LiNi 0.6 Co 0.2 Mn 0.2 O 2 –Mesocarbon Microbead Full Cells. *Energy Technol.* **7**, (2019).

89. Madec, L. *et al.* Understanding the Role of Prop-1-ene-1,3-Sultone and Vinylene Carbonate in LiNi 1/3 Mn 1/3 Co 1/3 O 2 /Graphite Pouch Cells: Electrochemical, GC-MS and XPS Analysis. *J. Electrochem. Soc.* **162**, A2635–A2645 (2015).

90. Zhu, Y., Casselman, M. D., Li, Y., Wei, A. & Abraham, D. P. Perfluoroalkyl-substituted ethylene carbonates: Novel electrolyte additives for high-voltage lithium-ion batteries. *J. Power Sources* **246**, 184–191 (2014).

91. Pham, H. Q., Nguyen, M. T., Tarik, M., El Kazzi, M. & Trabesinger, S. Cross-Talk-Suppressing Electrolyte Additive Enabling High Voltage Performance of Ni-Rich Layered Oxides in Li-Ion Batteries. *ChemSusChem* **14**, 2461–2474 (2021).

92. Li, L. *et al.* Recent progress on electrolyte functional additives for protection of nickel-rich layered oxide cathode materials. *Journal of Energy Chemistry* vol. 65 280–292 (2022).

93. Liu, H. *et al.* Understanding the Roles of Tris(trimethylsilyl) Phosphite (TMSPi) in LiNi0.8Mn0.1Co0.1O2 (NMC811)/Silicon–Graphite (Si–Gr) Lithium-Ion Batteries. *Adv. Mater. Interfaces* **7**, (2020).

94. Dong, H. & Koenig, G. M. A review on synthesis and engineering of crystal precursors produced: Via coprecipitation for multicomponent lithium-ion battery cathode materials. *CrystEngComm* vol. 22 1514–1530 (2020).

95. Liang, C. *et al.* Site-dependent multicomponent doping strategy for Ni-rich LiNi1-2: YCoyMnyO2 (y = 1/12) cathode materials for Li-ion batteries. *J. Mater. Chem. A* **5**, 25303–25313 (2017).

96. Park, K. J. *et al.* Improved Cycling Stability of Li[Ni0.90Co0.05Mn0.05]O2 Through Microstructure Modification by Boron Doping for Li-Ion Batteries. *Adv. Energy Mater.* **8**, (2018).

97. Li, C. *et al.* Inducing Favorable Cation Antisite by Doping Halogen in Ni-Rich Layered Cathode with Ultrahigh Stability. *Adv. Sci.* **6**, 1801406 (2019).

98.   Liu, Q., Wang, S., Tan, H., Yang, Z. & Zeng, J. Preparation and doping mode of doped LiMn2O4 for Li-ion batteries. *Energies* vol. 6 1718–1730 (2013).

99.   Wei, Y. J. *et al.* Effects of Ni doping on [MnO6] octahedron in LiMn 2O4. *J. Phys. Chem. B* **108**, 18547–18551 (2004).

100.   Chen, L. *et al.* Mechanism for Al2O3 Atomic Layer Deposition on LiMn2O4 from In Situ Measurements and Ab Initio Calculations. *Chem* **4**, 2418–2435 (2018).

101.   Jun, D. W., Yoon, C. S., Kim, U. H. & Sun, Y. K. High-Energy Density Core-Shell Structured Li[Ni0.95Co0.025Mn0.025]O2 Cathode for Lithium-Ion Batteries. *Chem. Mater.* **29**, 5048–5052 (2017).

102.   George, S. M. Atomic layer deposition: An overview. *Chem. Rev.* **110**, 111–131 (2010).

103.   Weckman, T. & Laasonen, K. First principles study of the atomic layer deposition of alumina by TMA-H2O-process. *Phys. Chem. Chem. Phys.* **17**, 17322–17334 (2015).

104.   Aarik, J., Aidla, A., Mändar, H. & Uustare, T. Atomic layer deposition of titanium dioxide from TiCl4 and H2O: Investigation of growth mechanism. *Appl. Surf. Sci.* **172**, 148–158 (2001).

105.   Xie, M. *et al.* Amorphous Ultrathin TiO 2 Atomic Layer Deposition Films on Carbon Nanotubes as Anodes for Lithium Ion Batteries. *J. Electrochem. Soc.* **162**, A974–A981 (2015).

106.   Strmcnik, D. *et al.* Electrocatalytic transformation of HF impurity to H2 and LiF in lithium-ion batteries. *Nat. Catal.* **1**, 255–262 (2018).

107.   Borodin, O. *et al.* Modeling Insight into Battery Electrolyte Electrochemical Stability and Interfacial Structure. *Acc. Chem. Res.* **50**, 2886–2894 (2017).

108.   Andersson, J. M. Linköping Studies in Science and Technology Controlling the Formation and Stability of Alumina Phases. *Department of Physics, Chemistry, and Biology* vol. Linköping (2005).

109.   Wei, A., He, R., Zhang, L. & Liu, Z. Enhancing the electrochemical performance of LiNi0.5Mn1.5O4 by V2O5-modification for Li-ion batteries. in *Journal of Physics: Conference Series* vol. 1605 (2020).

110.   Groner, M. D., Fabreguette, F. H., Elam, J. W. & George, S. M. Low-Temperature Al2O3 Atomic Layer Deposition. *Chem. Mater.* **16**, 639–645 (2004).

111.   Piercy, B. D., Leng, C. Z. & Losego, M. D. Variation in the density, optical polarizabilities, and crystallinity of TiO 2 thin films deposited via atomic layer deposition from 38 to 150 °C using the titanium tetrachloride-water reaction. *J. Vac. Sci. Technol. A Vacuum, Surfaces, Film.* **35**, 03E107 (2017).

112.   Daubert, J. S. *et al.* Intrinsic limitations of atomic layer deposition for pseudocapacitive metal oxides in porous electrochemical capacitor electrodes. *J. Mater. Chem. A* **5**, 13086–13097 (2017).

113.   Fares, C. *et al.* Band offset determination for amorphous Al2O3deposited on bulk AlN and atomic-layer epitaxial AlN on sapphire. *Appl. Phys. Lett.* **117**, 182103 (2020).

114.   Nolan, A. M., Wickramaratne, D., Bernstein, N., Mo, Y. & Johannes, M. D. Li+Diffusion in Amorphous and Crystalline Al2O3for Battery Electrode Coatings. *Chem. Mater.* **33**, 7795–7804 (2021).

115. Kang, D., Warburton, R. E., Mane, A. U., Greeley, J. & Elam, J. W. Modification of LiMn2O4 Surfaces by Controlling the Acid–Base Surface Chemistry of Atomic Layer Deposition. *Appl. Surf. Sci.* 153329 (2022) doi:10.1016/j.apsusc.2022.153329.

116. Baggetto, L., Dudney, N. J. & Veith, G. M. Surface chemistry of metal oxide coated lithium manganese nickel oxide thin film cathodes studied by XPS. *Electrochim. Acta* **90**, 135–147 (2013).

117. Xu, G., Liu, Z., Zhang, C., Cui, G. & Chen, L. Strategies for improving the cyclability and thermo-stability of LiMn2O4-based batteries at elevated temperatures. *Journal of Materials Chemistry A* vol. 3 4092–4123 (2015).

118. Waller, G. H. *et al.* Structure and surface chemistry of Al2O3 coated LiMn2O4 nanostructured electrodes with improved lifetime. *J. Power Sources* **306**, 162–170 (2016).

119. Gallus, D. R. *et al.* The influence of different conducting salts on the metal dissolution and capacity fading of NCM cathode material. *Electrochim. Acta* **134**, 393–398 (2014).

120. Schmidt, H. & Noack, J. Elektrolysen von Perchloraten. I. Elektrolysen an Ag-, Cu- und Pt-Anoden in Acetonitril. *ZAAC - J. Inorg. Gen. Chem.* **296**, 262–272 (1958).

121. Krtil, P., Kavan, L. & Novák, P. Oxidation of Acetonitrile-Based Electrolyte Solutions at High Potentials: An In Situ Fourier Transform Infrared Spectroscopy Study. *J. Electrochem. Soc.* **140**, 3390–3395 (1993).

122. Hunter, J. C. Preparation of a new crystal form of manganese dioxide: λ-MnO2. *J. Solid State Chem.* **39**, 142–147 (1981).

123. Metzger, M., Strehle, B., Solchenbach, S. & Gasteiger, H. A. Hydrolysis of Ethylene Carbonate with Water and Hydroxide under Battery Operating Conditions. *J. Electrochem. Soc.* **163**, A1219–A1225 (2016).

124. Borodin, O., Olguin, M., Spear, C. E., Leiter, K. W. & Knap, J. Towards high throughput screening of electrochemical stability of battery electrolytes. *Nanotechnology* **26**, 354003 (2015).

125. Leung, K. First-Principles Modeling of the Initial Stages of Organic Solvent Decomposition on LixMn2O4(100) Surfaces. *J. Phys. Chem. C* **116**, 9852–9861 (2012).

126. Giordano, L. *et al.* Chemical Reactivity Descriptor for the Oxide-Electrolyte Interface in Li-Ion Batteries. *J. Phys. Chem. Lett.* **8**, 3881–3887 (2017).

127. Zhang, Y. *et al.* Revealing electrolyte oxidation: Via carbonate dehydrogenation on Ni-based oxides in Li-ion batteries by in situ Fourier transform infrared spectroscopy. *Energy Environ. Sci.* **13**, 183–199 (2020).

128. Xu, M., Tsiouvaras, N., Garsuch, A., Gasteiger, H. A. & Lucht, B. L. Generation of cathode passivation films via oxidation of lithium bis(oxalato) borate on high voltage spinel (LiNi0.5Mn 1.5O4). *J. Phys. Chem. C* **118**, 7363–7368 (2014).

129. Fang, S., Jackson, D., Dreibelbis, M. L., Kuech, T. F. & Hamers, R. J. Anode-originated SEI migration contributes to formation of cathode-electrolyte interphase layer. *J. Power Sources* **373**, 184–192 (2018).

130. Buchberger, I. *et al.* Aging Analysis of Graphite/LiNi 1/3 Mn 1/3 Co 1/3 O 2 Cells Using XRD, PGAA, and AC Impedance. *J. Electrochem. Soc.* **162**, A2737–A2746 (2015).

131. Yang, X. *et al.* Mechanism of cycling degradation and strategy to stabilize a nickel-rich cathode. *J. Mater. Chem. A* **6**, 16149–16163 (2018).

132. Wang, C. *et al.* Lithium Difluorophosphate As a Promising Electrolyte Lithium Additive for High-Voltage Lithium-Ion Batteries. *ACS Appl. Energy Mater.* **1**, 2647–2656 (2018).

133. Dong, L. *et al.* Stabilization of high-voltage lithium metal batteries using a sulfone-based electrolyte with bi-electrode affinity and LiSO2F-rich interphases. *Energy Storage Mater.* **44**, 527–536 (2022).

134. Ma, L. *et al.* A Guide to Ethylene Carbonate-Free Electrolyte Making for Li-Ion Cells. *J. Electrochem. Soc.* **164**, A5008–A5018 (2017).

135. Logan, E. R. *et al.* A Study of the Transport Properties of Ethylene Carbonate-Free Li Electrolytes. *J. Electrochem. Soc.* **165**, A705–A716 (2018).

136. Björklund, E., Göttlinger, M., Edström, K., Younesi, R. & Brandell, D. Sulfolane-Based Ethylene Carbonate-Free Electrolytes for LiNi0.6Mn0.2Co0.2O2−Li4Ti5O12 Batteries. *Batter. Supercaps* **3**, 201–207 (2020).

137. Ruff, Z., Xu, C. & Grey, C. P. Transition Metal Dissolution and Degradation in NMC811-Graphite Electrochemical Cells. *J. Electrochem. Soc.* **168**, 060518 (2021).

138. Wandt, J. *et al.* Transition metal dissolution and deposition in Li-ion batteries investigated by operando X-ray absorption spectroscopy. *J. Mater. Chem. A* **4**, 18300–18305 (2016).

139. Tan, S. *et al.* Additive engineering for robust interphases to stabilize high-Ni layered structures at ultra-high voltage of 4.8 V. *Nat. Energy* **7**, 484–494 (2022).

140. Wang, C. *et al.* High-voltage LiNi0.4Co0.4Mn0.2O2/graphite pouch battery cycled at 4.5 V with a LiDFP-based electrolyte. *Ionics (Kiel).* **27**, 4135–4142 (2021).

141. Zhao, W. *et al.* Toward a stable solid-electrolyte-interfaces on nickel-rich cathodes: LiPO2F2 salt-type additive and its working mechanism for LiNi0.5Mn0.25Co0.25O2 cathodes. *J. Power Sources* **380**, 149–157 (2018).

142. Klein, S. *et al.* On the Beneficial Impact of Li2CO3 as Electrolyte Additive in NCM523 ‖ Graphite Lithium Ion Cells Under High-Voltage Conditions. *Adv. Energy Mater.* **11**, (2021).

143. Jung, R. *et al.* Nickel, Manganese, and Cobalt Dissolution from Ni-Rich NMC and Their Effects on NMC622-Graphite Cells. *J. Electrochem. Soc.* **166**, A378–A389 (2019).

144. Tochihara, M. *et al.* Liquid Chromatography-Quadruple Time of Flight Mass Spectrometry Analysis of Products in Degraded Lithium-Ion Batteries. *J. Electrochem. Soc.* **162**, A2008–A2015 (2015).

145. Plakhotnyk, A. V., Ernst, L. & Schmutzler, R. Hydrolysis in the system LiPF 6 - Propylene carbonate - Dimethyl carbonate - H 2O. *J. Fluor. Chem.* **126**, 27–31 (2005).

146. Li, R. *et al.* Enhanced high voltage performance of LiNi0.5Mn0.3Co0.2O2cathodeviathe synergistic effect of LiPO2F2and FEC in fluorinated electrolyte for lithium-ion batteries. *RSC Adv.* **11**, 7886–7895 (2021).

Acta Universitatis Upsaliensis

Digital Comprehensive Summaries of Uppsala Dissertations
from the Faculty of Science and Technology 2178

Editor: The Dean of the Faculty of Science and Technology